The roles of yeast formins and their regulators Bud6 and Bil2 in the pheromone response

Joseph O. Magliozzi[a], Thomas J. Rands[a], Sudati Shrestha[b], William C. Simke[b], Niklas E. Hase[b], M. Angeles Juanes[a,c], Joshua B. Kelley[b], and Bruce L. Goode[a,*]

[a]Department of Biology, Brandeis University, Waltham, MA 02454; [b]Department of Molecular and Biomedical Sciences, University of Maine, Orono, ME 04469; [c]Centro de Investigación Príncipe Felipe, 46012 Valencia, Spain

ABSTRACT **In response to pheromone *Saccharomyces cerevisiae* extend a mating projection. This process depends on the formation of polarized actin cables which direct secretion to the mating tip and translocate the nucleus for karyogamy. Here, we demonstrate that proper mating projection formation requires the formin Bni1, as well as the actin nucleation promoting activities of Bud6, but not the formin Bnr1. Further, Bni1 is required for pheromone gradient tracking. Our work also reveals unexpected new functions for Bil2 in the pheromone response. Previously we identified Bil2 as a direct inhibitor of Bnr1 during vegetative cell growth. Here, we show that Bil2 has Bnr1-independent functions in spatially focusing Bni1-GFP at mating projection tips, and in vitro Bil2 and its binding partner Bud6 organize Bni1 into clusters that nucleate actin assembly. *bil2*Δ cells also display entangled Bni1-generated actin cable arrays and defects in secretory vesicle transport and nuclear positioning. At low pheromone concentrations, *bil2*Δ cells are delayed in establishing a polarity axis, and at high concentrations they prematurely form a second and a third mating projection. Together, these results suggest that Bil2 promotes the proper formation and timing of mating projections by organizing Bni1 and maintaining a persistent axis of polarized growth.**

Monitoring Editor
Sophie Martin
Université de Genève

Received: Nov 30, 2023
Revised: Apr 9, 2024
Accepted: Apr 17, 2024

New Hypothesis

SIGNIFICANCE STATEMENT

- Formins and their regulators have been studied for many years in yeast, but almost exclusively in mitotically dividing cells, leaving their roles in the pheromone response poorly understood.
- The authors here find that proper shmoo formation requires the formin Bni1 but not Bnr1, as well as the actin nucleation-promoting activities of Bud6, and a novel activity of Bil2 in spatially organizing Bni1 at mating projection tips.
- This work demonstrates the physiological importance of formin spatial regulation in shaping actin networks, which in turn shapes cell morphology, and establishes an ideal in vivo system for dissecting Bni1 regulation.

This article was published online ahead of print in MBoC in Press (http://www.molbiolcell.org/cgi/doi/10.1091/mbc.E23-11-0459) on April 24, 2024.

*Address correspondence to: Dr. Bruce L. Goode (goode@brandeis.edu).

Abbreviations used: GFP, green fluorescent protein; MBP, maltose binding protein; RFP, red fluorescent protein; SIM, structured illumination microscopy; SoRa, superresolution by optical pixel reassignment; TIRF, total internal reflection fluorescence.

INTRODUCTION

The ability of cells to polarize in response to chemical gradients is crucial for a wide range of cellular and physiological processes (Drubin and Nelson, 1996; Ghose *et al*., 2022). Budding yeast *Saccharomyces cerevisiae* has long served as a powerful model for dissecting the molecular underpinnings of polarity establishment (Chiou *et al*., 2017). In budding yeast, polarity is specified during mitotic growth by an asymmetric cortical landmark established during the previous cell division. This spatial cue initiates a signaling cascade at one end of the cell, leading to polarized actin cable

assembly, which steers secretion in the direction of the polarity site to promote bud growth (Moseley and Goode, 2006; Chiou *et al.*, 2017). Formins play an essential role in polarized cell growth. They are activated at the polarity site to assemble linear actin structures called "cables" that extend into the mother cell and serve as tracks for myosin-based transport of secretory vesicles and other cargos to the bud tip. This establishes a cortical exocytic (or secretion) zone at the bud tip, which becomes corralled by endocytic (cortical) actin patches (Jose *et al.*, 2013, 2015). The patches are crucial for the retrieval and internalization of components from the plasma membrane, which keeps the polarity site tightly focused (Jose *et al.*, 2013).

The majority of our knowledge about the regulated assembly of actin cables and patches in yeast comes from studies on vegetatively growing cells (going through cycles of bud formation and mitotic division). Less is known about how actin assembly is regulated during the reproductive cycle of yeast. During mating, haploid cells of opposite mating type (MATa and MATα) secrete pheromones to attract each other and fuse, forming diploids, which subsequently undergo meiosis and sporulation to reform haploids (Merlini *et al.*, 2013). Because *S. cerevisiae* are nonmotile, successful mating requires a dramatic change in cell morphology (called "shmooing"), in which cells extend a mating projection in the direction of their mating partner to promote cell–cell contact. When this is achieved, cell wall degradation occurs at the cell contact site, followed by plasma membrane fusion, cytoplasmic mixing, and finally nuclear fusion (karyogamy) to form diploids. This cascade of events is initiated by haploid MATa and MATα cells secreting mating pheromones (a-factor and α-factor, respectively) to establish gradients. These pheromones bind to receptors (GPCRs) in the plasma membranes of cells of the opposite mating type, which leads to activation of Cdc42 at the incipient shmoo tip. Cdc42 and its effectors in turn recruit and activate the formin Bni1 to this site, which leads to the polymerization of actin cables that direct secretion and facilitate mating projection extension (Evangelista *et al.*, 1997; Matheos *et al.*, 2004).

Upon exposure to a low concentration gradient of pheromone, cells respond by extending a single mating projection in the direction of the gradient. However, cells exposed to a high (uniform) concentration of pheromone, which saturates the pheromone receptors, they "default" to forming a first mating projection from the site of a cortical landmark remaining from the last cell division (Wang *et al.*, 2019). Under these conditions, after 2–3 h, when the first mating projection is not successful in contacting a mating partner, a second and then a third mating projection is extended in different directions in an effort to find a mating partner (Merlini *et al.*, 2013). This "repetitive shmooing" behavior has been noted for many years, and has been ascribed to an independent transcriptional oscillator (Haase and Reed, 1999; Orlando *et al.*, 2008), a MAPK oscillator (Hilioti *et al.*, 2008), and a Cdc42 cycle (Bidlingmaier and Snyder, 2004). Presumably, these signaling pathways act upstream of formins, and possibly other actin cytoskeletal machinery, to direct polarized secretion and thus control the timing of mating projection formation.

In vegetatively growing yeast cells, two genetically-redundant formins (Bni1 and Bnr1) share the load in polymerizing actin cable networks, with Bni1 spatially positioned at the bud tip through most of the cell cycle, and Bnr1 at the bud neck (Pruyne *et al.*, 2004). A genetic disruption in either formin alone leads to modest changes in cell growth and morphology, whereas loss of both formins is lethal (Imamura *et al.*, 1997). One unfortunate consequence of this genetic redundancy in formins is that the effects of disrupting a gene that governs the activities of only one formin can be masked by the presence of the other formin in the cell. In contrast, during the mating response formation of a proper mating projection depends on just one formin (Bni1). Loss of Bnr1 causes no obvious defects in mating (Gao and Bretscher, 2009), and loss of Bni1 results in abnormally shaped mating projections and defects in mating (Matheos *et al.*, 2004; Bidlingmaier and Snyder, 2004; Miller *et al.*, 1999). These properties make the yeast mating pathway a potentially powerful system for elucidating mechanisms specifically regulating Bni1.

The N-terminal half of Bni1 contains a Cdc42-binding site and a diaphanous inhibitory domain (DID), while the C-terminal half of Bni1 (C-Bni1) consists of the formin-homology FH1 and FH2 domains followed by a tail region that contains the diaphanous autoregulatory domain (DAD). In vitro, C-Bni1 is sufficient to nucleate actin polymerization (Sagot *et al.*, 2002b; Pruyne *et al.*, 2002) and remains attached to the growing barbed ends of filaments during elongation, accelerating their growth in a profilin-dependent manner and protecting filament ends from capping protein (Moseley *et al.*, 2004; Kovar, 2006). While the activities of C-Bni1 are well documented, until now the activities of full-length Bni1 (FL-Bni1) have not been reported. It has been proposed that FL-Bni1 is autoinhibited, based in part on it containing DID and DAD domains, which in many other formins mediate autoinhibition (Evangelista *et al.*, 2002; Sagot *et al.*, 2002a; Li and Higgs, 2003, 2005). Autoinhibition of Bni1 has also been suggested by the observation that expressing truncated Bni1 constructs (lacking DID or DAD domains) produces numerous short actin cables in vivo (Evangelista *et al.*, 1997, 2002; Sagot *et al.*, 2002a; Kono *et al.*, 2012). Importantly however, these same phenotypes can arise from the truncations disrupting "transinhibition" mechanisms rather than autoinhibition, and Bni1 autoinhibition has never been verified in vitro. Further, there are clear exceptions to the DID-DAD autoinhibition rule, as purified full-length mammalian formin INF2, which has DID and DAD domains, is constitutively active rather than autoinhibited (A *et al.*, 2019). Instead, INF2 is transinhibited by a complex consisting of cyclase-associated protein 2 (CAP2) and acetylated G-actin, which bind to the formin DID and DAD domains, respectively. Thus, formin activity can be negatively regulated by either auto- or transinhibitory mechanisms, and determining which mechanisms apply to a specific formin requires biochemical characterization of the purified full-length protein.

Bud6 is a cell polarity factor with roles in regulating actin cable formation, orienting the mitotic spindle, and maintaining membrane boundaries between cellular compartments (Ozaki-Kuroda *et al.*, 2001; Martin *et al.*, 2007; Ten Hoopen *et al.*, 2012; Graziano *et al.*, 2013; Clay *et al.*, 2014). The specific role of Bud6 in promoting actin cable formation is that it serves as a nucleation promoting factor (NPF) for the formins Bni1 and Bnr1. C-terminal fragments of Bud6, C-Bud6(L)$^{489–788}$ and C-Bud6(S)$^{550–788}$ bind to the C-terminal tail region of C-Bni1 (FH1-FH2-C) and enhance its actin nucleation activities (Graziano *et al.*, 2011, 2013). C-Bud6(L)$^{489–788}$ and C-Bud6(S)$^{550–788}$ each contain a dimeric "core" (550–688) that binds to the tail region of Bni1 near the DAD domain (Moseley and Goode, 2005; Tu *et al.*, 2012). Adjacent to the formin-binding core domain is a flanking region (689–788) that contains a WH2-like actin monomer-binding domain (Moseley *et al.*, 2004; Park *et al.*, 2015). Point mutations in Bud6 that disrupt its interactions with either Bni1 (e.g., *bud6-35*) or G-actin (e.g., *bud6-8*) abolish its NPF effects in vitro, and result in diminished actin cable staining in vivo similar to *bud6*Δ (Moseley *et al.*, 2004; Moseley and Goode, 2005; Graziano *et al.*, 2011; Tu *et al.*, 2012; Graziano *et al.*, 2013; Park *et al.*, 2015). To date, all biochemical characterization of Bud6's NPF activities have relied on either C-Bud6(L)$^{489–788}$ and C-Bud6(S)$^{550–788}$ fragments, and the activity of full-length Bud6 (FL-Bud6) has remained

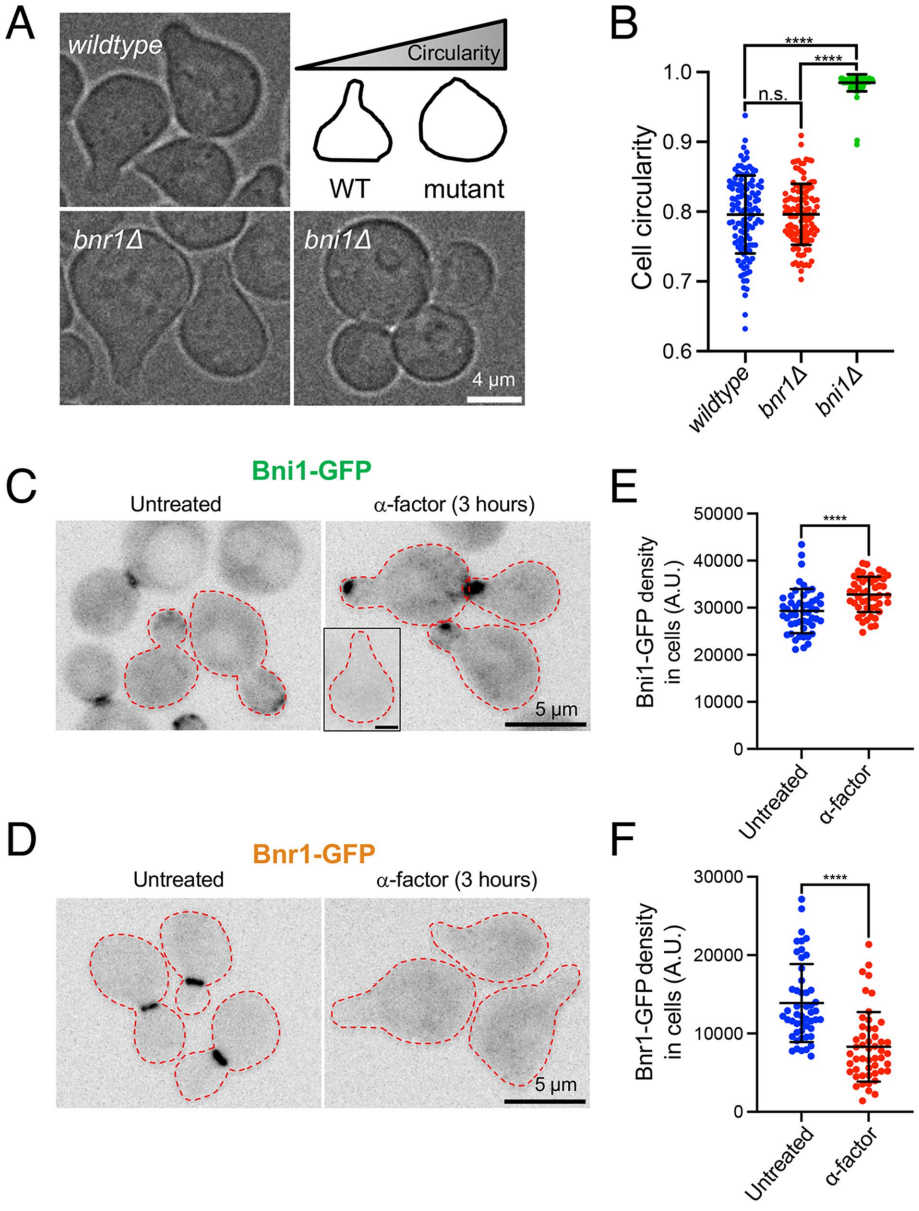

FIGURE 1: Bni1 and Bnr1 protein levels, localization, and genetic requirements during the pheromone response. (A) Representative brightfield images of cells 3 h after treatment with pheromone (100 μM alpha factor). Inset, cartoon comparing a wildtype (WT) cell extending a mating projection and a mutant cell defective in this process, leading to its increased circularity index. (B) Cell circularity measurements (mean ± SD). Data from three independent trials ($n = 120$ cells per strain). ****$p < 0.0001$, n.s. not significant by Tukey's ANOVA. (C) Representative images of endogenously-tagged Bni1-GFP in untreated cells and cells treated for 3 h with alpha factor (100 μM). Inset shows the control (untagged) strain used to establish subtracted background fluorescence. Scale bar: 2 μm. (D) Representative images of endogenously-tagged Bnr1-GFP as above for Bni1-GFP. (E) Quantification of Bni1-GFP fluorescence density (mean ± SD) in cells before and after treatment with 100 μM alpha factor for 3 h. Data from three independent trials ($n = 50$ cells per strain). ****$p < 0.0001$ by Tukey's ANOVA. (F) Quantification of Bnr1-GFP fluorescence density (mean ± SD) in cells before and after treatment with 100 μM alpha factor for 3 h. Data from three independent trials ($n = 50$ cells per strain). ****$p < 0.0001$ by Tukey's ANOVA.

unexplored. In addition to its NPF effects on Bni1, Bud6 serves as an NPF for Bnr1; however, this specifically requires an additional factor, Bud6-interacting ligand (Bil1; Graziano *et al.*, 2013). Bil1 is a small protein (9 kDa) binds to a regulatory region of Bud6 (489–550) and unmasks Bud6's NPF effects on Bnr1.

Recently, we identified another small binding partner of Bud6, which we named Bil2 (15 kDa; Rands and Goode, 2021). We found that Bil2 inhibits Bnr1- but not Bni1-mediated actin nucleation in vitro. Further, we showed that in vegetatively growing cells Bil2 colocalizes with Bud6 at polarity sites (bud cortex and bud neck) and is required for proper architecture of Bnr1-nucleated actin cables in vivo. In the present study, we investigated whether Bil2 has functions during the mating response and uncovered a new and unexpected role for Bil2 in controlling the spatial organization of Bni1 at mating projection tips and the timing of mating projection formation under both high and low pheromone concentrations. Further, we show that these new functions of Bil2 during the pheromone response are Bnr1-independent. Thus, Bil2 has two distinct formin regulatory roles in yeast, inhibiting Bnr1 activity during vegetative growth and focusing Bni1 localization during the mating response.

RESULTS

Expression and localization of Bni1 and Bnr1 during the mating response

We were interested in studying the roles of formins and their regulators during the pheromone response, and started by examining the roles of Bni1 and Bnr1 in our strain background (W303). After exposure to a high concentration of pheromone for 3 h, *bni1*Δ cells failed to form a mating projection, whereas *bnr1*Δ cells were indistinguishable from wildtype cells (Figure 1A). Quantification of cell circularity supported this conclusion, as formation of mating projections in wildtype and *bnr1*Δ cells decreased their circularity indexes (Figure 1B). Our results for Bnr1 were in good agreement with previous studies performed in the S288C background; however, our results for Bni1 were different than what has been reported (Gao and Bretscher, 2009). Specifically, previous studies showed that *bni1*Δ cells in the S288C background form mating projections, although abnormal shape (Bidlingmaier and Snyder, 2004; Gao and Bretscher, 2009). Interestingly, one study performed in the W303 background reported that *bni1*Δ cells "fail to polarize, remain ellipsoidal, and contain delocalized cortical actin patches" (Matheos *et al.*, 2004). Given these discrepancies, we directly compared shmoo formation for wild-type and *bni1*Δ cells in the W303 and S288C backgrounds. After 3 h of exposure to pheromone W303 *bni1*Δ cells failed to extend a mating projection, whereas S288C *bni1*Δ cells extended an abnormally broad projection (Supplemental Figure S1A). By 5 h, W303 *bni1*Δ cells had begun to extend projections, but they were

comparatively short and stubby. Therefore, clear differences exist between the strain backgrounds in how severely the loss of *BNI1* affects mating projection formation. All experiments herein, unless otherwise specified, are performed in the W303 background.

In addition, we confirmed that wildtype cells from W303 and S288C backgrounds treated with latrunculin B could grow only very short mating projections, although these cells did undergo some form of polarized growth (Supplemental Figure S1B) as reported previously (Hegemann *et al.*, 2015).

We next examined Bni1 and Bnr1 localization during the mating response using endogenously tagged formins with an enhanced variant of GFP (GFP^{ENVY}) optimized for detection and photostability in yeast (Slubowski *et al.*, 2015). Previous studies have shown that integrated C-terminal GFP tags do not interfere with Bni1 or Bnr1 function (Buttery *et al.*, 2007). In vegetatively growing cells, we found that Bni1-GFP localized to many discrete puncta, which were found throughout the cytosol but were enriched at the bud cortex (Figure 1C), as seen previously (Buttery *et al.*, 2007). In cells exposed to a high concentration of pheromone, Bni1-GFP was focused to a single spot near the mating projection tip as expected (Matheos *et al.*, 2004). For Bnr1, there was little information in the literature about its expression levels or localization during the mating response. In mitotically dividing cells, we observed Bnr1-GFP predominantly at the bud neck (Figure 1D), consistent with its known interactions with septins and septin-binding proteins (Buttery *et al.*, 2007, 2012; Gao *et al.*, 2010). After exposure to a high concentration of pheromone, we observed Bnr1-GFP in the cytosol, and it was no longer at any discrete structures, including cortical septin striations. A control parent strain (lacking any GFP tag) was used for comparison to define background fluorescence (see inset, Figure 1C), demonstrating that the cytosol Bnr1-GFP signal is specific. Interestingly, in shmoos treated acutely (10 min) with latrunculin B, a fraction of the Bnr1-GFP shifted to cortical dots (Supplemental Figure S1C), organized in a pattern resembling septin striations in pheromone-treated yeast (Longtine *et al.*, 1998a). Thus, the cytosolic localization of Bnr1 during the mating response appears to be F-actin dependent. This differs considerably from Bnr1-GFP in vegetatively growing cells, where its localization to the bud neck is independent of F-actin and dependent on septins (Buttery *et al.*, 2007, 2012; Gao *et al.*, 2010).

We also assessed the cellular levels of Bni1-GFP and Bnr1-GFP before and after exposure to pheromone. We measured total GFP intensities from full z-stacks through cells (sum projection) after background subtraction and normalized signals for cell area. This yielded fluorescence density, which reflects protein concentration in the cells. Whereas the concentration of Bni1 in cells increased slightly (Figure 1E), the concentration of Bnr1 decreased to approximately half the normal level after pheromone treatment (Figure 1F). Thus, despite not contributing to mating projection formation genetically, Bnr1 is present during the mating response, but at reduced levels found in the cytosol. Together, these observations indicate that Bni1 is the dominant formin in the mating response. Further, they raise new questions about why Bnr1 no longer stably localizes to septins during the mating response, and instead resides in the cytosol (see *Discussion*).

Loss of *BIL2* leads to unexpected defects in mating projection formation

Because Bni1 is the only formin required for proper mating projection formation, we anticipated that Bil2, which in vitro inhibits Bnr1 but not Bni1, might not have any role in the mating response. However, after exposing cells to pheromone for 3 h, we found that *bil2*Δ cells extended a second and sometimes a third mating projection, whereas in the same period of time nearly all wildtype cells extended only a single mating projection (Figure 2, A and B). By later time points, wildtype cells "caught up" with *bil2*Δ cells and formed multiple mating projections as previously reported (Bücking-Throm *et al.*, 1973; Bidlingmaier and Snyder, 2004). These previous studies suggested that when cells extend mating projections that fail to get close enough to another cell to result in fusion, they redirect polarity to a new site and build a new mating projection. Our observations suggest that the loss of *BIL2* leads to these events occurring prematurely, and therefore Bil2 appears to be required for a normal commitment to one polarity axis during shmoo formation. Importantly, *bnr1*Δ*bil2*Δ cells showed the same phenotype as *bil2*Δ, while *bnr1*Δ cells were similar to wildtype cells (Supplemental Figure S2, A and B), demonstrating that the mating functions of Bil2 are independent of Bnr1.

To better understand this new function of Bil2, we next asked whether *bil2*Δ cells abandon their first mating projection upon initiating a second one, or alternatively they attempt to build two mating projections simultaneously. To address this, we used live imaging to compare secretory vesicle localization (GFP-Sec4) in wildtype and *bil2*Δ cells responding to pheromone. In wildtype cells, there is short (~10 min) overlap period during which the "old" mating projection and the new mating projection are both active followed by full commitment to the new projection (Bidlingmaier and Snyder, 2004; Matheos *et al.*, 2004). To assess whether *bil2*Δ might alter this overlap period, we used live imaging to examine mCherry-Sec4 localization and actin cable staining (Abp140-GFP). We considered a mating projection to be "active" whether there was clear GFP-Sec4 accumulation at its tip (Figure 2C) and actin cables extending from the tip (Figure 2D). Based on these criteria, *bil2*Δ cells showed a prolonged overlap period of simultaneous activity at older and newer mating projection tips (Supplemental Figure S2C). These observations reinforce the view that *bil2*Δ cells are defective in committing to a single polarity axis at a time, possibly explaining why they prematurely forms a second and a third mating projection.

Bud6 and Bil2 have distinct roles in promoting mating projection formation

Because Bud6 is a binding partner of Bil2, we next compared wildtype, *bil2*Δ, and *bud6*Δ cell morphologies after exposure to pheromone for 3 h. As above, *bil2*Δ cells had more mating projections compared with wildtype cells, but the projections tended to be slightly shorter, presumably because they fail to stably commit to one projection at a time (Figure 3A). The net effect of these two phenotypes (shorter, but increased number of projections) is that *bil2*Δ cells have circularity indexes similar to wildtype cells despite their morphological differences (Figure 3B). In contrast to wildtype cells, *bud6*Δ cells had shorter and broader mating projections, and did not display the *bil2*Δ phenotype of increased number of projections. As a result, *bud6*Δ cells have an increased circularity index compared with wildtype and *bil2*Δ cells, albeit not to the same extent as *bni1*Δ cells (Figure 3B). Interestingly, *bil2*Δ*bud6*Δ double mutant cells displayed a combination of defects seen in *bud6*Δ and *bil2*Δ cells, that is, shorter and broader mating projections along with increased number of projections. Together, these observations suggest that Bud6 and Bil2 each play important roles in shmoo formation, and that at least some of the roles they play are independent of one another.

We also asked whether the shmoo defects in *bud6*Δ cells result from the loss Bud6's NPF effects on Bni1. To address this question, we examined cells expressing integrated *bud6-35* and *bud6-8* point

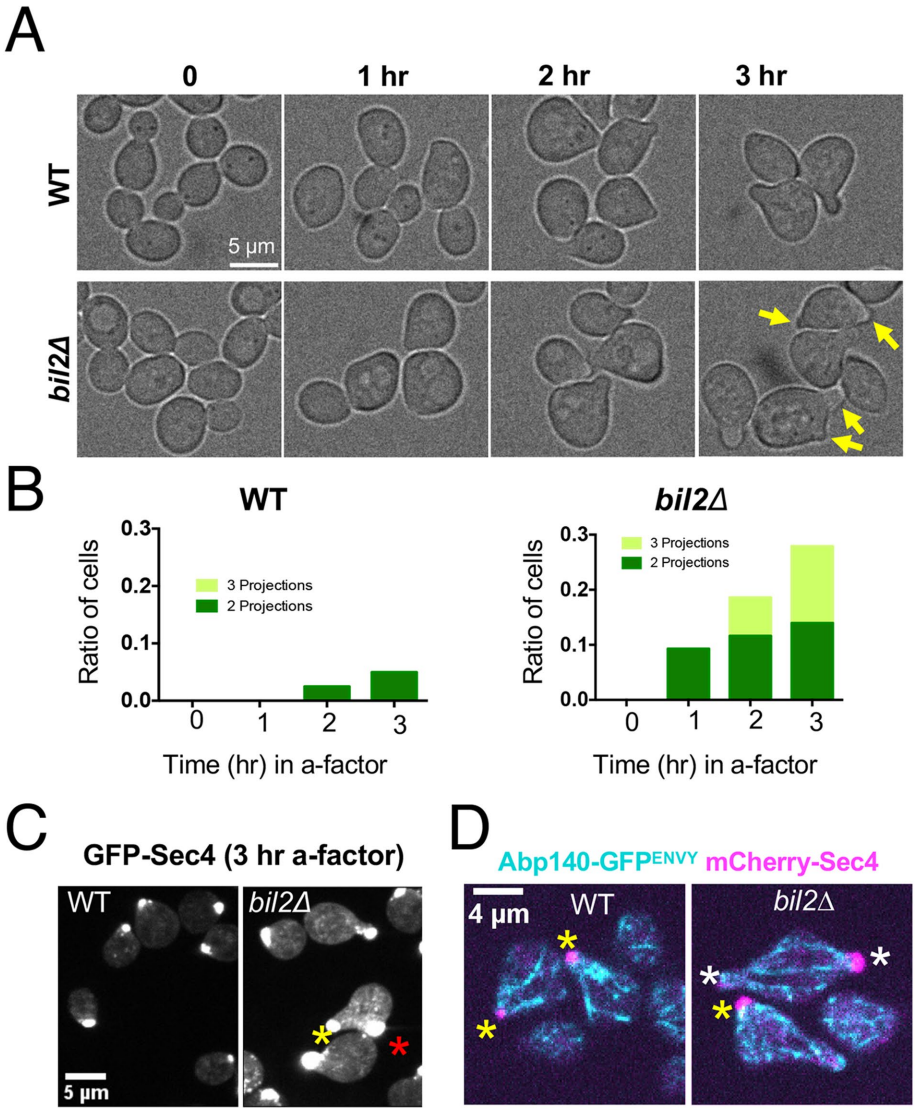

FIGURE 2: *bil2*Δ cells prematurely extend a second and/or a third mating projection during the pheromone response. (A) Representative brightfield images of wildtype (WT) and *bil2*Δ cells responding to alpha factor (100 μM). Yellow arrows indicate cells with multiple mating projections. (B) Percentage of cells ($n = 50$ cells per condition; from three independent trials) with a second and/or third mating projection at time points after exposure to 100 μM alpha factor. (C) Representative images showing GFP-Sec4 accumulation at polarity sites in wildtype and *bil2*Δ cells exposed to 100 μM alpha factor for 3 h. In the image for *bil2*Δ, one of the cells has two separate polarity sites, highlighted by yellow and red asterisks. (D) Representative live images showing actin cables (Abp140-GFP) and secretory vesicles (mCherry-Sec4) in wildtype and *bil2*Δ cells exposed to 100 μM alpha factor for 2 h. Yellow asterisks, cells with a single active polarity site. White asterisks, cells with two simultaneously-active polarity sites.

mutants, which specifically disrupt Bud6-formin and Bud6-actin interactions, respectively, and abolish its NPF activities in vitro (Graziano *et al.*, 2011). The *bud6-35* and *bud6-8* mutants showed similar shmoo defects to *bud6*Δ (Figure 3, A and B), suggesting that this phenotype results from the loss of Bud6 NPF effects on formins.

Overall, these observations indicate that Bni1 plays the central role in actin assembly underlying mating projection formation, while Bud6 facilitates this function by serving as an NPF for Bni1. Bil2 is not required for shaping the projection, but has an important role in limiting cells to a single site of polarized growth and thus building only a single mating projection at a time.

Loss of *BIL2* gives rise to entangled actin cable networks during the pheromone response

To better understand how the loss of *BIL2* destabilizes the polarity axis, we compared actin cable organization in wildtype, *bil2*Δ and *bud6*Δ cells after pheromone treatment. *bud6*Δ cells showed diminished cable staining (Figure 4A), similar to what has previously been described for *bud6*Δ in mitotically dividing cells (Graziano *et al.*, 2011). In contrast, cable staining was not diminished in *bil2*Δ cells (Figure 4A). Instead, traces of individual cables and overall cable staining revealed an increase in cable tortuosity (length/distance) and cable entanglement in *bil2*Δ but not *bud6*Δ cells (Figure 4, B and C). Because cables serve as tracks for secretory vesicle transport, distortions of cable shape can reduce the efficiency of vesicle traffic, which has been demonstrated for mutations in several different formin regulators (Eskin *et al.*, 2016; Garabedian *et al.*, 2018; Rands and Goode, 2021). Live imaging in wildtype cells revealed that secretory vesicles (GFP-Sec4) are transported to mating projection tips at a rate of ~15 vesicles/min (Figure 4D). This is similar to the ~14 vesicles/min transport rate to the bud tip in mitotically dividing cells (Rands and Goode, 2021). However, vesicle delivery frequencies to the shmoo tip were markedly reduced (~7–8 vesicles/min) in *bil2*Δ cells, consistent with the defects seen in actin cable organization in *bil2*Δ cells.

To further probe the cause of the actin cable entanglement in *bil2*Δ cells, we performed live imaging on cables using an integrated Abp140-GFP marker. Previous studies showed that cables in *hof1*Δ cells have increased tortuosity, which appears to be caused by altered angles of cable extension when cables emerge from the bud neck and enter the mother cell compartment (Garabedian *et al.*, 2020). We asked whether *bil2*Δ cables might have similar defects. Therefore, we tracked the extending ends of cables for several microns from the mating projection tip into the cell body and measured the angles of cable extension with respect to the mating projection axis (see cartoon, Figure 4E). Wildtype and *bil2*Δ cables showed similar initial cable extension angles (Figure 4E), suggesting that the increased cable tortuosity in *bil2*Δ cables is unlikely to arise from defects in the initial phase of cable extension. Further analysis revealed that indeed, it is the distal portions of the cables (from the center of the cell to the back of the cell) that are more tortuous in *bil2*Δ cells (Figure 4F). These observations suggest that loss of *BIL2* alters cable architecture in a way that results in cable bending and/or buckling.

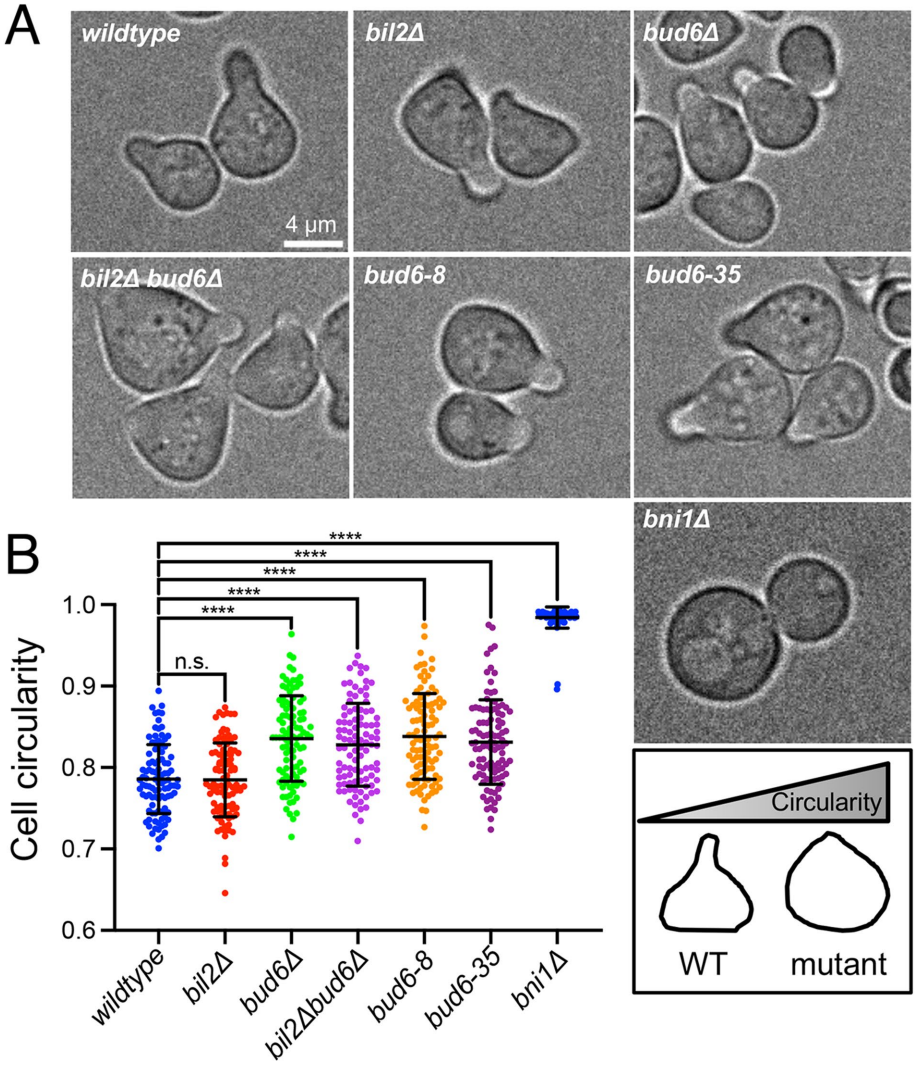

FIGURE 3: Distinct defects in shmoo morphology for *bud6*Δ and *bil2*Δ. (A) Representative brightfield images of cells 3 h after exposure to 100 μM alpha factor. Scale bar, 4 μm. Inset, cartoon comparing a wildtype (WT) cell extending a mating projection versus a mutant cell defective in this process which leads to its increased circularity index. (B) Cell circularity measurements (mean ± SD). Data from three trials ($n = 100$ cells per strain). ****$p < 0.0001$, n.s. not significant by Dunnet's ANOVA.

Bil2 is required for proper nuclear positioning in cells responding to pheromone

During the mating response, the nucleus moves up to into the mating projection with its spindle pole body pointing towards the tip of the mating projection (Hasek *et al.*, 1987; Rose and Fink, 1987; Palmer *et al.*, 1992). Further, actin cables are required for microtubule-dependent translocation of the nucleus toward the shmoo tip to facilitate karyogamy after cell fusion (Read *et al.*, 1992; Rose, 1996). Therefore, we also asked whether Bil2 is important for nuclear positioning. To address this, we used established live imaging assays with endogenously tagged Spc72-GFP to compare the distance of the microtubule organizing center (spindle pole body) from mating projection tips in wildtype and *bil2*Δ cells (Figure 5, A and B). As a complementary approach, we used endogenously tagged TUB1-GFP to compare the distance from the middle of the nuclear microtubule bundle to the mating projection tip in wildtype and *bil2*Δ cells (Figure 5, C and D). The results from both sets of experiments demonstrate that *bil2*Δ compromises nuclear positioning, which in turn suggests that proper cable architecture is critical not only for normal rates of secretory vesicle transport (Figure 4D) but also for nuclear migration.

Bni1-GFP disappears from the first mating projection tip prematurely in *bil2*Δ cells

Given the effects of *bil2*Δ on actin cable organization, we asked whether Bil2 influences Bni1 localization in vivo. To accomplish this, we used the endogenously-tagged Bni1-GFP constructs described earlier (Figure 1), and compared their localization patterns in wildtype and *bil2*Δ cells 2.5 h after exposure to a high dose (100 μM) of mating pheromone (Figure 6, A and B). In wildtype and *bud6*Δ cells, Bni1-GFP was concentrated in a single spot at the tip of the first mating projection. In contrast, in many *bil2*Δ cells Bni1-GFP localization was split, with remnants at the first mating projection tip and less tightly focused signal at the new location on the cell cortex where a new mating projection was emerging. We confirmed that *bil2*Δ does not change Bni1-GFP levels in cells (Figure 6C), and that similar changes in Bni1-GFP localization are seen in *bil2*Δ and *bil2*Δ*bud6*Δ cells (Figure 6, A and B), and in *bil2*Δ*bnr1*Δ cells double mutants (Supplemental Figure S2, D and E). Thus, the role of Bil2 in spatially localizing Bni1 is independent of Bud6 or Bnr1.

We also asked whether Bil2 colocalizes with Bni1 in mating cells. We were limited in what probe we could use to monitor Bil2 localization, because we previously showed that endogenously-tagged Bil2-GFP fails to complement *BIL2* function, and that is undetectable by light microscopy (Rands and Goode, 2021). However, in that study we showed that an N-terminally tagged GFP-Bil2 fusion protein (expressed from a low copy plasmid with a constitutive promoter) complements *BIL2* function and localizes to polarity sites. Therefore, we introduced the same GFP-Bil2 plasmid into cells expressing endogenously-tagged Bni1-mScarlet to ask whether Bil2 and Bni1 colocalize during mating. Bni1 and Bil2 each displayed a high level of cytosolic staining with clear enrichment at the mating projection tips (Figure 6D). Another study showed a similar pattern for Bni1-GFP in mitotically-dividing cells, where Bni1-GFP exhibited a high level of cytosolic staining but was enriched at the bud tip (Buttery *et al.*, 2007). In that study, the authors showed that after treating cells with latrunculin, Bni1-GFP became more enriched at the bud tip, suggesting that actin polymerization promotes dissociation of Bni1-GFP from the cortex (back into the cytoplasm). Therefore, we asked whether latrunculin treatment might have a similar effect on Bni1-mScarlet and/or GFP-Bil2 in mating cells. Indeed, we found that both Bni1-mScarlet and GFP-Bil2 were more enriched at mating tips after latrunculin treatment (Figure 6E). Note that ~20% of the cells expressing Bni1-mScarlet showed staining in the vacuole (as reflected in the three out of 11 cells combined in Figures 6, D and E),

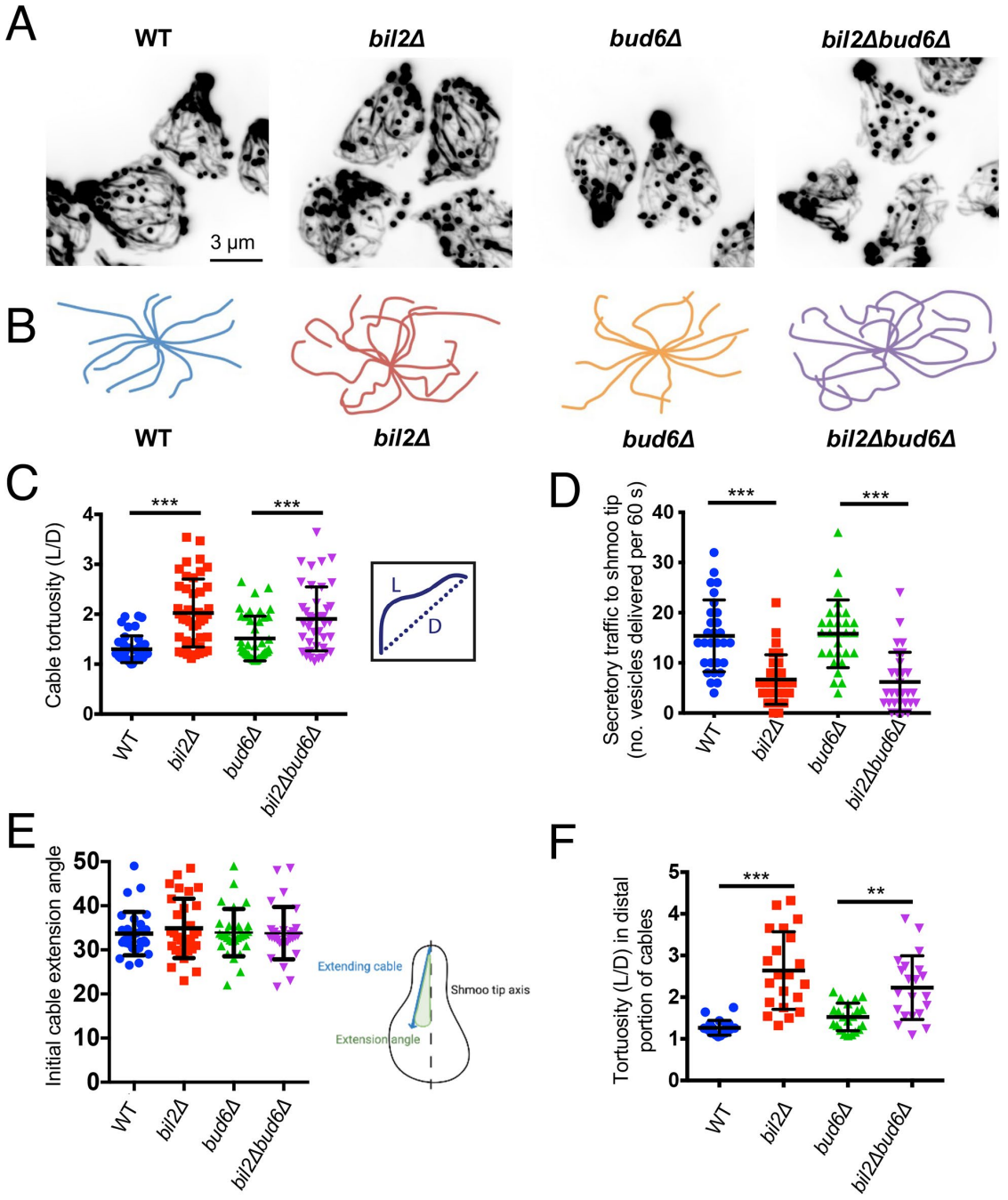

FIGURE 4: Bil2 is required for normal actin cable organization and secretory vesicle transport during the pheromone response. (A) Representative SoRa images showing F-actin organization in cells exposed to 100 μM alpha-factor for 3 h. Cells were fixed and stained with Alexa-488-phalloidin. (B) Representative actin cable traces (12 per condition), where the central dot corresponds to the end of the cable at the mating projection tip. (C) Actin cable tortuosity (L/D) (mean ± SD), quantified by measuring the length of each cable manually in FIJI and dividing the length by the distance from beginning to end. Each dot represents one cable. Data from three trials ($n > 30$ cables per condition). (D) Frequency of secretory vesicle delivery to shmoo tip. Live imaging was used to quantify the number of vesicles (marked with GFP-Sec4) successfully transported to within 2.5 μm of the mating projection tip per minute (mean ± SD). Data from three independent trials. Each data point is from one cell ($n = 40$ cells per condition). (E) Initial extension angle of actin cable growth (mean ± SD) measured by live cell imaging of endogenously-tagged Abp140-GFP. Actin cables were observed and marked in FIJI as they extended from the mating projection tips, and the angle was compared with the longitudinal axis drawn from the mating tip to the back of the cell. Data from three trials ($n = 45$ cables per condition). Right, cartoon illustrating cable extension angle. (F) Cable tortuosity (L/D) in distal half of the cables. Data from three trials ($n = 21$ cables per condition). Statistical significance calculated by two-way student *t* test in all panels. $^{**}p \leq 0.01$, $^{***}p \leq 0.001$.

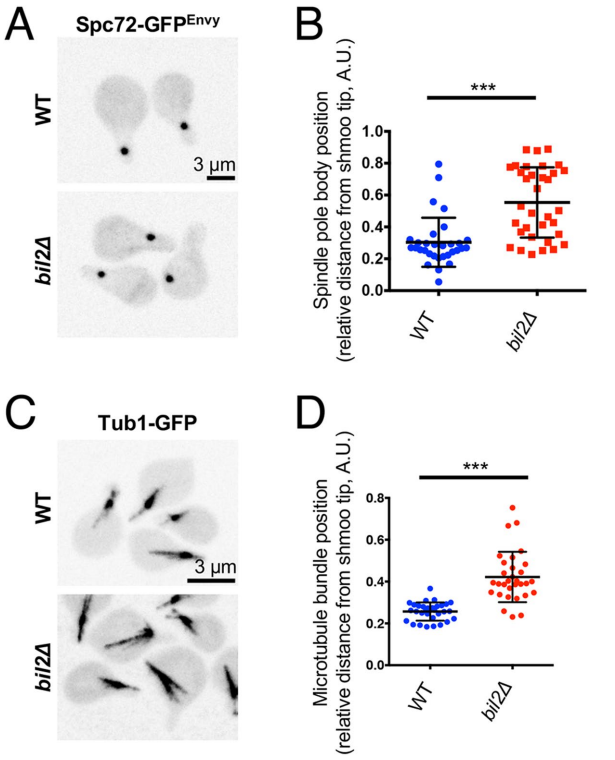

FIGURE 5: Bil2 is required for proper nuclear positioning during the pheromone response. (A) Example images of cells expressing an endogenously-tagged (GFP^{Envy}) Spc72 (spindle pole body marker) exposed to 100 μM alpha factor for 3 h. Images are maximum intensity projections of z-stacks. (B) Distance from the tip of the mating projection to the center of the spindle pole body (Spc72-GFP^{Envy}; mean ± SD) was analyzed as described (Manatschal *et al.*, 2016), dividing this distance by the total length of the cell (from the mating projection tip to the back of the cell). Data from three independent trials ($n = 35$ cells per strain). ***$p < 0.001$ by two-way student *t* test. (C) Representative images of cells expressing endogenously-tagged Tub1-GFP exposed to 100 μM alpha factor for 3 h. Images are maximum intensity projections of z-stacks. (D) Distance from the tip of the mating projection to the center of the nuclear microtubule bundle (Tub1-GFP; mean ± SD) analyzed as described (Manatschal *et al.*, 2016), dividing this distance by the total length of the cell defined as above. Data from three independent trials ($n = 35$ cells per strain). ***$p < 0.001$ by two-way student *t*-test.

which may result from prolonged exposure to pheromone. Together, these results suggest that Bil2 is able to colocalize with Bni1 at mating projection tips, and together with the defects in actin cable organization observed in *bil2*Δ cells, suggests a possible role for Bil2 in regulating Bni1 localization and/or activity during the mating response.

Bil2 spatially focuses Bni1-GFP and stabilizes the polarity axis in pheromone gradients

To gain additional insights into the role of Bil2 during the mating response, we next employed a microfluidics-assisted live-cell imaging assay to compare wildtype and *bil2*Δ cells responding to a low concentration gradient of pheromone (0–150 nM; Moore *et al.*, 2008; Kelley *et al.*, 2015). This differs from our experiments above where cells were exposed to a uniform high concentration of pheromone (100 μM). Pheromone gradients are thought to more closely mimic conditions found in nature, where cells respond to a low-level gradient of pheromone being secreted by a nearby cell of the opposite mating type. In this assay, strains are compared for their abilities to reorient their polarity axis and extend a mating projection in the direction of the gradient.

The ability of yeast to track a gradient is dependent upon local activation of Cdc42 by pheromone receptors (GPCRs/Ste4) at the cortex. This requires Fus3 kinase phosphorylation of Far1, which then couples the Cdc42 GEF (Cdc24) to the Gβ subunit of GPCR (Alvaro and Thorner, 2016). Gradient tracking also relies on the α subunit of GPCR (Gpa1), which scaffolds Fus3 (Errede *et al.*, 2015). The Gpa1-Fus3 complex phosphorylates Bni1, which promotes polarized actin cable assembly and gradient tracking (Matheos *et al.*, 2004; Yu *et al.*, 2008). Despite these links between the signaling components of the pheromone response and Bni1, to our knowledge the role of Bni1 in gradient tracking has never been tested. In these experiments, we compared wildtype, *bil2*Δ, and *bud6*Δ cells in the W303 background to be consistent with all of the experiments above. However, we chose to analyze *bni1*Δ and *bnr1*Δ in the S288C background given the enhanced pheromone-induced polarized growth of *bni1*Δ cells in this background compared with W303 (Supplemental Figure S1A).

Using a microfluidic gradient chamber, we examined cells in a 0–150 nM pheromone gradient. W303 wildtype cells tracked the gradient efficiently (Figure 7, A and B), as we have previously showed for S288C wildtype cells (Kelley *et al.*, 2015). In contrast, *bni1*Δ cells were highly defective in gradient tracking, while *bnr1*Δ cells were indistinguishable from wildtype. While *bni1*Δ cells were able to eventually elongate (after ~5–8 h) under these conditions, that is, grow in a polarized manner, it is important to note that the orientation of their growth was random. Thus, *bni1*Δ cells are unable to steer cell growth toward a gradient. Interestingly, gradient tracking in *bud6*Δ and *bil2*Δ cells (scored after 8 h in the gradient) appeared to be similar to wildtype cells (Figure 7A). However, during the time course of these gradient assays, we noticed that *bil2*Δ cells were delayed in establishing a persistent axis of polarized growth. To further address this, we performed a separate experiment in which we quantified the time to establishment of polarity in cells expressing endogenously tagged Bni1-GFP and Bem1-mRuby exposed to a flat low concentration of pheromone (100 nM) sufficient to drive elongated growth. Gradients were not used in this experiment, because a flat concentration of pheromone yields a much larger number of cells that can be analyzed, because every cell experiences the same dose of pheromone. Time to stable polarity establishment was defined as the time at which a persistent cell projection first appeared. In wildtype and *bud6*Δ cells, Bni1-GFP formed a tight cap that moved along the cell periphery for a period of time and then established a stable position, accompanied by the formation of a mating projection (Supplemental Figure 3A; Figure 7C). However, in *bil2*Δ cells the Bni1-GFP polarity cap wandered for an extended period of time (~100 min longer than wildtype or *bud6*Δ cells) before establishing a persistent polarity axis and extending a projection (Figure 7C). In addition, we compared Bni1-GFP and Bem1-mRuby distribution patterns in wildtype and *bil2*Δ cells exposed to an intermediate concentration of pheromone (300 nM) adequate to drive mating projection formation. In wildtype cells, Bni1-GFP and Bem1-mRuby formed tightly focused spots at the mating projection tips, whereas in *bil2*Δ cells they had more diffusive localization patterns (Supplemental Figure 3B). In addition, *bil2*Δ cells showed a significant increase in the number of Bni1-GFP foci compared with wildtype cells (Figure 7D). Thus, Bil2 is required for stabilizing pheromone-induced polarized growth. It is possible that these defects stem, at least in part, from an inability of *bil2*Δ cells to focus Bni1 at mating projection tips. This could lead

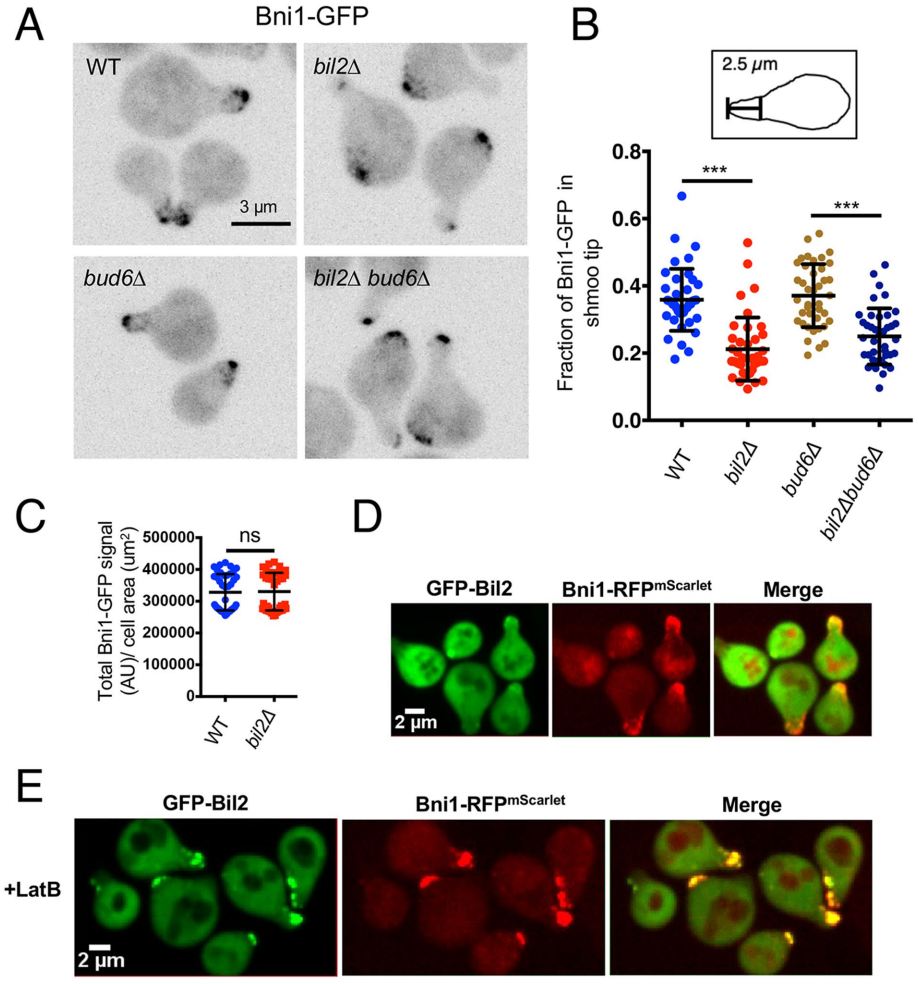

FIGURE 6: Bni1-GFP localization is altered in *bil2*Δ cells responding to pheromone. (A) Representative images of Bni1-GFP localization in cells exposed to 100 μM alpha factor for 2.5 h. Images are sum intensity projections of z-stacks. (B) Fraction of total Bni1-GFP signal in the cell (mean ± SD) located within 2.5 μm of the shmoo tip. Data from three independent trials ($n = 30$ cells per strain). ***$p < 0.001$ by two-way student *t* test. (C) Quantification of Bni1-GFP fluorescence density (mean ± SD, $n = 30$ cells per strain) in wildtype and *bil2*Δ cells after 2.5 h exposure to 100 μM alpha factor. ns = not significant by two-way student *t* test. (D) Representative images of cells with endogenously-tagged Bni1-RFP^{mScarlet} and pGFP-Bil2 expressed from a low copy plasmid after 2.5 h exposure to 100 μM alpha factor. Images are sum intensity projections of z-stacks. (E) Same as D, but cells were treated with 100 μM Latrunculin for 10 min before imaging.

to dispersed (unfocused) exocytosis, and in turn dispersed Bem1 localization.

Bil2 and Bud6 spatially cluster Bni1 molecules in vitro to nucleate actin asters

Given our in vivo results showing that Bil2 spatially focuses Bni1 at mating projection tips and influences actin cable architecture, we decided to carefully examine whether purified Bil2 has any regulatory effects on Bni1-mediated actin assembly in vitro. In our previous in vitro work, we had shown that Bil2 inhibits Bnr1- but not Bni1-mediated actin assembly in bulk assays (Rands and Goode, 2021). Here, we examined the effects of purified Bil2, alone and together with Bud6, on Bni1-mediated actin assembly in both bulk assays (Figure 8A) and total internal reflection fluorescence (TIRF) microscopy assays (Figure 8B). We used FL-Bni1 and FL-Bud6 (Supplemental Figure S4A), rather than their C-terminal fragments, because we did not know what regions of Bni1 and/or Bud6 might be required for Bil2 to exert regulatory effects. Note that the activities of FL-Bni1 and FL-Bud6 have not previously been reported. In bulk actin assembly assays, FL-Bud6 showed similar stimulatory (NPF) effects on C-Bni1 and FL-Bni1 (Supplemental Figure S4B). These NPF effects of FL-Bud6 were similar to those reported for C-Bud6 (Moseley *et al.*, 2004; Graziano *et al.*, 2011, 2013), suggesting that most of the NPF activity of Bud6 resides in its C-terminal half (489–788).

A comparison of FL-Bni1 and C-Bni1 activities revealed that they have similar actin nucleation effects in bulk assays over a wide concentration range (Supplemental Figure S4C), as well as similar effects in TIRF assays in accelerating filament elongation in the presence of profilin (Supplemental Figure S4D). These observations demonstrate that FL-Bni1 is constitutively active, despite the presence of its DID and DAD domains (see *Introduction*). In this respect, FL-Bni1 may be similar to the mammalian formin INF2, which has DID and DAD domains yet is constitutively active, and is inhibited *in trans* by other cellular factors that bind to its DID and DAD domains (A *et al.*, 2019). Interestingly, the effects of ΔDID and ΔDAD mutations in Bni1 in vivo (Evangelista *et al.*, 1997, 2002; Sagot *et al.*, 2002b; Kono *et al.*, 2012), which have always been interpreted as supporting Bni1 autoinhibition, equally support a transinhibitory mechanism (see *Discussion*).

In bulk and TIRF assays, Bil2 alone displayed minimal effects on FL-Bni1 nucleation activity (Figure 8, A and B), consistent with our previous observations for Bil2 with C-Bni1 (Rands and Goode, 2021). In addition, we observed bright actin puncta in TIRF reactions containing Bil2, consistent with our previous work on Bil2, where it was shown that the puncta are comprised of G-actin (Rands and Goode, 2021). FL-Bud6 alone enhanced FL-Bni1-mediated actin nucleation activity similar to our previously described NPF effects of C-Bud6 on C-Bni1 (Moseley *et al.*, 2004; Graziano *et al.*, 2011). The further addition of Bil2 (together with FL-Bud6) led to a small increase in FL-Bni1 nucleation activity. Note, this is in stark contrast to Bil2's inhibitory effects on Bnr1-mediated actin nucleation both in the presence and absence of C-Bud6 (Rands and Goode, 2021). Thus, Bil2 differentially regulates the two formins, inhibiting nucleation by Bnr1 and slightly enhancing nucleation by Bni1.

In our TIRF experiments we also noticed the formation of actin "asters" (clusters of actin filaments polymerizing out of discrete foci) in reactions that specifically contained Bil2, FL-Bud6, and FL-Bni1, and to a lesser extent reactions containing FL-Bud6 and FL-Bni1 (no Bil2; Figure 8, C and D). Asters were never observed in reactions containing Bnr1 (instead of Bni1) with Bil2 and/or Bud6 (Rands and Goode, 2021). In addition, asters were not observed in reactions lacking FL-Bud6, indicating that in vitro Bil2 and FL-Bud6 together

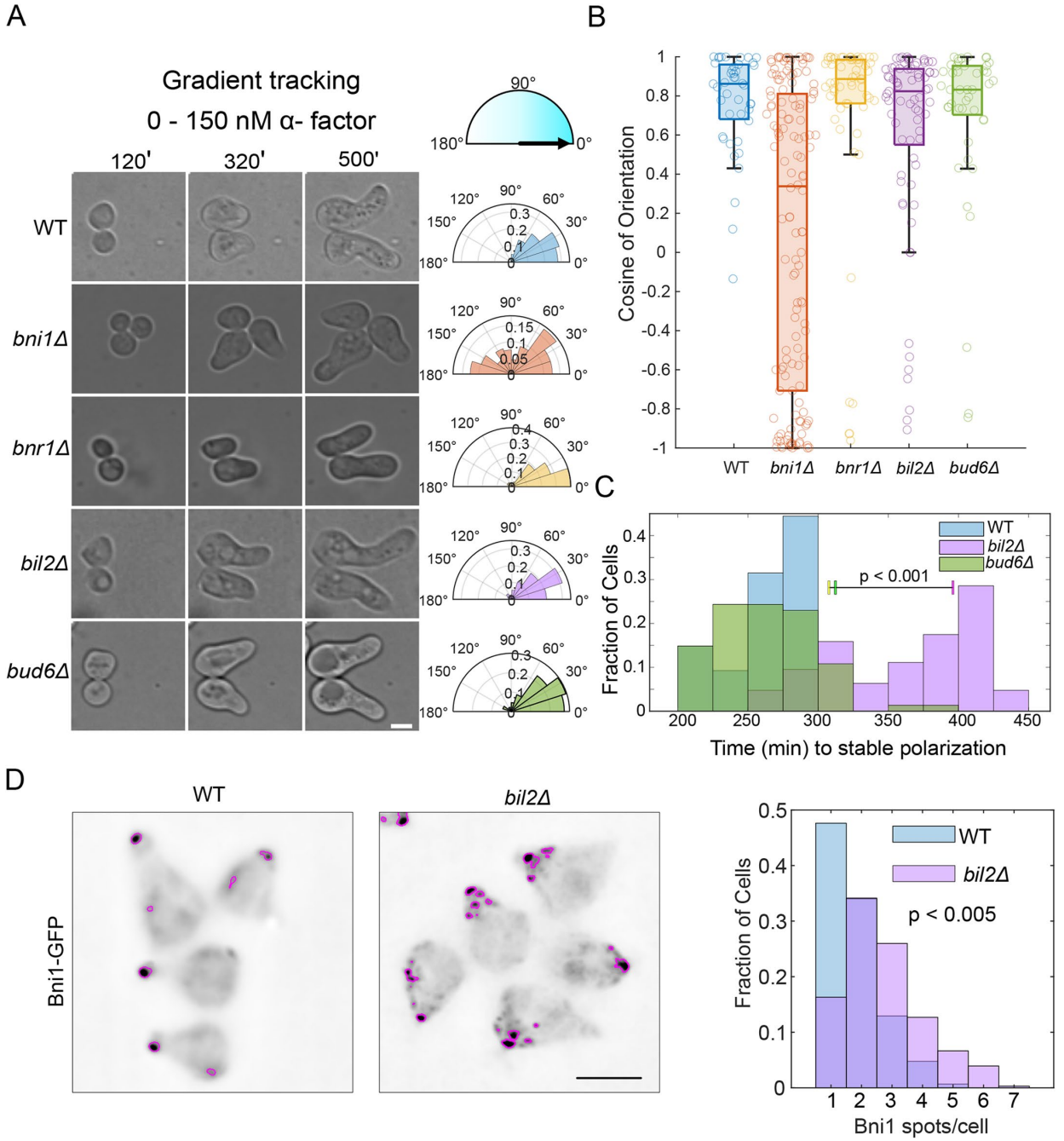

FIGURE 7: Bni1 is required for tracking pheromone gradients, and Bil2 is required for stabilizing the polarity axis and clustering Bni1-GFP at mating projection tips. (A) Representative images of WT, *bni1*Δ, *bnr1*Δ, *bil2*Δ and *bud6*Δ tracking a gradient of alpha factor (0–150 nM) in a microfluidic chamber for 12 h. Concentration of alpha factor is high on the right side and low on the left side. Scale bar: 5 μm. On the right are polar histograms (in degrees) of the final orientation of cells from the following strains: WT ($n = 43$), *bni1*Δ ($n = 134$), *bnr1*Δ ($n = 58$), *bil2*Δ ($n = 73$) and *bud6*Δ ($n = 84$) from two independent experiments. (B) Quantification of gradient tracking by plotting the cosine of the final angle of orientation. An average cosine approaching one indicates efficient tracking of the gradient, while an average cosine approaching zero represents random orientation of growth and a failure to track the gradient. (C) A histogram representing the fraction of cells that have established a stable polarity site by the indicated time in WT, *bil2*Δ and *bud6*Δ cells exposed to 100 nM alpha factor, sufficient to drive elongation but not shmoo formation (100 nM). WT ($n = 54$), *bil2*Δ ($n = 63$), and *bud6*Δ ($n = 74$) from two independent experiments. Statistical significance was assessed by pairwise Kolmogorov-Smirnov tests. (D) The numbers of Bni1-GFP spots in WT and *bil2*Δ cells exposed to 300 nM pheromone was compared using the Granulinator MATLAB script to identify spots that were three standard deviations above the average intensity of the cell. Examples of Bni1-GFP spots identified by Granulinator are circled in magenta. On the right is a histogram of the fraction of cells with the indicated number of spots in WT and *bil2*Δ cells. Statistical significance was assessed by a pairwise Kolmogorov-Smirnov test, with WT cells ($n = 153$) and *bil2*Δ cells ($n = 333$). Scale bar, 5 μm.

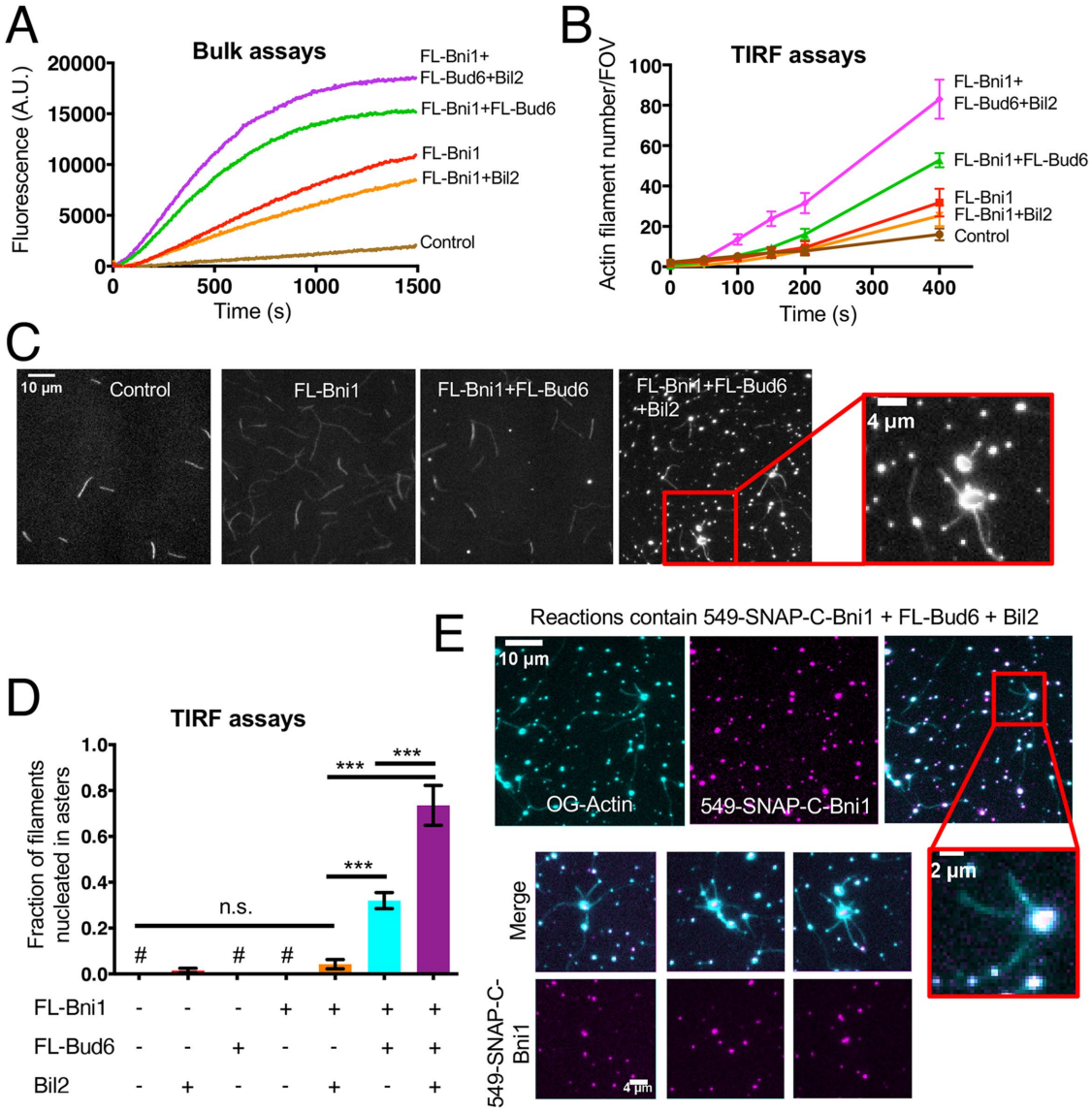

FIGURE 8: In vitro Bil2 and Bud6 cluster Bni1 to nucleate actin filament asters. (A) Bulk pyrene-actin assembly assays showing a modest stimulatory effect for Bil2 on FL-Bni1-mediated actin nucleation, both in the presence and absence of FL-Bud6. Reactions contain 2 µM actin monomers (5% pyrene-labeled), 5 µM profilin, and different combinations of 10 nM FL-Bni1, 100 nM FL-Bud6, and 100 nM Bil2. Data shown are one representative trial out of three. (B) Quantification of actin nucleation effects in TIRF assays. Number of filaments (mean ± SEM) nucleated per field of view (FOV) scored at the indicated time points in TIRF reactions. Reactions contain 1 µM actin monomers (10% labeled), 3 µM profilin, and different combinations of 2 nM FL-Bni1, 100 nM FL-Bud6, and 100 nM Bil2. (C) Representative FOVs from TIRF reactions 200 s after initiation of actin assembly, with zoom-in highlighting combined effects of Bil2 and Bud6 in organizing Bni1-nucleated asters. (D) Fraction of total filaments (mean ± SEM) in FOVs associated with asters. Data from 8 replicates per condition. (E) Representative images from reactions 200 s after initiation of actin assembly (and close ups of example asters), showing that Bil2 and Bud6 concentrate 549-SNAP-C-Bni1 at the centers of asters. Reactions contain 1 µM actin monomers (10% labeled), 3 µM profilin, 2 nM 549-SNAP-C-Bni1, 100 nM Bil2, and 100 nM FL-Bud6. Statistical significance calculated by two-way student *t* test in all panels (n.s., no significance, ***$p \leq 0.001$).

induce Bni1-dependent aster formation. We reasoned that the formation of asters could result from Bni1 being clustered at the centers of the asters, such that the pointed ends of actin filaments radiate from these centers. To test this idea, we repeated the assays with labeled 549-SNAP-C-Bni1 (FH1-FH2-C), which revealed that Bni1 is concentrated at the aster centers (Figure 8E). Interestingly, this spatial organization in vitro is similar to the organization of actin cable arrays observed in vivo, where Bni1 is in a spot at the mating projection tip and the pointed ends of the actin cables radiate from that spot. Thus, our in vitro assay has reconstituted some of the key aspects of the in vivo spatial organization of Bni1 and actin cable assembly.

DISCUSSION

In this study, we examined the roles of the two *S. cerevisiae* formins (Bni1 and Bnr1) and two known formin regulators (Bud6 and Bil2) during the pheromone response. Our direct comparison of latrunculin B and *bni1*Δ effects in the W303 and S288C strain

backgrounds demonstrates that actin is required to form proper mating projections, and that Bni1 plays a major role in shaping the mating projection. The mating projection defects for *bni1*Δ are more pronounced in the W303 background, which was used for most of the remaining experiments. Our data using *bud6-35* and *bud6-8* point mutants show that Bud6 facilitates mating projection formation by serving as a formin NPF, presumably for Bni1 because we could find no role for Bnr1 in this process. These results also agree with another recent study showing that *bud6*Δ cells have short, broad mating projections, as do cells carrying mutations in Bni1 that disrupt Bud6 binding (Lawson *et al.*, 2022). We found that Bni1 is required for tracking pheromone gradients, which to our knowledge has never been reported previously. Although *bni1*Δ cells could still elongate in response to a gradient, they could not steer growth toward the pheromone source. Thus, Bni1 is critical for tracking gradients at lower concentrations of pheromone (0–150 nM), and for properly building mating projections at higher concentrations of pheromone (100 μM), while Bud6 plays a more facilitative role as an NPF for Bni1.

Our work also reveals new and unexpected roles for Bil2 in the pheromone response. Previously, Bil2 was shown to inhibit Bnr1 but not Bni1 activity (Rands and Goode, 2021). However, here we discovered that Bil2 spatially focuses Bni1 into a tight spot at mating projection tips, and that this function is independent of Bnr1. Consistent with this function, *bil2*Δ cells display defects in actin cable organization, leading to defects in secretory vesicle transport and nuclear positioning. The inability to properly focus Bni1 and organize actin cable arrays may also explain why *bil2*Δ cells exposed to high concentrations of pheromone abort their first mating projection and begin extending a second and then a third projection prematurely. Specifically, these defects in maintaining a persistent polarity axis in *bil2*Δ cells may stem from unfocused exocytosis. In addition, we observed that *bil2*Δ cells exposed to lower concentrations of pheromone have defects in establishing a tight polarity axis, as indicated by Bem1-mRuby. In addition, we found that purified Bil2 (together with Bud6) organizes Bni1 into clusters in vitro, from which actin filaments polymerize. Together, these observations support a role for Bil2 during the pheromone response in promoting Bni1 clustering to organize actin cable arrays and stabilize polarized growth. Importantly, we have demonstrated that these new functions of Bil2 are independent of Bnr1. However, we cannot rule out the possibility that some of these functions of Bil2 in the mating response are through formin-independent mechanisms.

It is also worth noting that we could find no genetic role for Bnr1 in shmoo formation, yet Bnr1 was expressed during the mating response, albeit at approximately half of the normal Bnr1 levels expressed in vegetatively growing cells. During the mating response, Bnr1 was cytosolic, suggesting that Bnr1 no longer stably associates with septins. A previous study showed that during G1 in mitotically dividing cells (before bud emergence), Bnr1 is inactive and cytosolic (Yu *et al.*, 2011), and upon bud emergence, Bnr1 is then recruited by septins to the bud neck where it becomes active and assembles actin cables (Gao *et al.*, 2010; Buttery *et al.*, 2012). Because exposure to mating pheromone leads to a G1 arrest, it is possible that a related mechanism inactivates Bnr1 in both settings, perhaps involving cell cycle regulated changes in septins and/or septin-associated proteins (Juanes and Piatti, 2016). Interestingly, when we treated pheromone-induced cells briefly with latrunculin, a fraction of the Bnr1-GFP shifted from the cytosol to cortical dots, which showed a striated organization similar to septins in mating cells (Longtine *et al.*, 1998a). These observations show that the rules governing Bnr1 localization during the mating response differ considerably from those governing its stable localization to the bud neck during vegetative growth.

How would Bni1 clustering relate to the establishment of a stable polarity axis?

Wandering of the polarity cap (marked by Bem1) is driven by exocytosis (Ozaki-Kuroda *et al.*, 2001; Dyer *et al.*, 2013). Vesicles travel along actin cables to reach the site of exocytosis where delivery of inactive signaling molecules perturbs the polar cap. With tightly clustered Bni1, actin cables would all emanate from approximately the same spatial position, resulting in focused exocytosis. In the absence of Bil2, the Bni1 spot disperses into multiple foci. In this situation, exocytic events may also be spread out, leading to scattered exocytosis and changes to polar cap spatial dynamics. Exocytosis provides negative regulation of the polar cap by delivering inactive polarity signaling components to the center of the polarity patch; however, it also provides a delayed positive feedback, as the arrival of the new signaling molecules (once they are activated) reinforces the signal. This produces a signal that can pull the polar cap back to the site of vesicle delivery, slowing polar cap wandering in a dose dependent manner (McClure *et al.*, 2015). Defocusing of the actin cable assembly sites, marked by Bni1-GFP, may therefore create multiple competing polarity spots, leading to the observed effect of destabilizing the polarity axis.

The observation that the polarity cap is more mobile at lower doses of pheromone and less mobile at higher doses (Dyer *et al.*, 2013) may be related to our observation of delayed mating projection extension in *bil2*Δ cells at lower doses of pheromone. This suggests that Bil2 may be more important for spatially focusing Bni1 at the mating projection tips when the polarity cap is highly mobile. Consistent with this view, *bil2*Δ cells exhibited a dispersal of Bni1-GFP and a delay in mating projection formation at low (100–300 nM) but not high (100 μM) concentrations of pheromone.

In vitro activities of FL-Bni1, Bud6 and Bil2

In this study, we have characterized for the first time the in vitro activities of FL-Bni1 and Bud6, and the effects of Bil2 on FL-Bni1 and Bud6. FL-Bud6 (1–788) shows a similar NPF activity to C-terminal fragments of Bud6 (489–788 and 550–788), demonstrating that the C-terminal half of Bud6 contains most or all of the NPF activity. More unexpectedly, we found that FL-Bni1, despite containing DID and DAD domains, is constitutively active for actin assembly rather than autoinhibited. As mentioned earlier, it has long been assumed that Bni1 is autoinhibited based on ΔDID and ΔDAD phenotypes in vivo (Evangelista *et al.*, 1997, 2002; Sagot *et al.*, 2002b; Kono *et al.*, 2012). However, these phenotypes are also consistent with Bni1 being inhibited *in trans* by ligands that interact with the DID and DAD domains, as recently shown for mammalian formin INF2 (A *et al.*, 2019). Future studies will be needed to identify the inhibitory factors bound to Bni1 in the cytosol, and determine how they are released when Bni1 is activated at the bud cortex.

In a previous study employing bulk assays in vitro, we showed that Bil2 inhibits actin nucleation by Bnr1 but not Bni1, either in the presence and absence of Bud6 (Rands and Goode, 2021). Here, using TIRF microscopy we discovered that Bil2 and Bud6 together organize Bni1 into clusters that nucleate actin filament assembly into asters. These in vitro results mirror the in vivo requirement for Bil2 in focusing Bni1-GFP at mating projection tips. On the other hand, the requirement of Bud6 in our in vitro assays is seemingly at odds with the in vivo observation that *bud6*Δ cells do not have the same phenotype as *bil2*Δ cells. However, this could easily be explained whether this

role of Bud6 (in helping Bil2 concentrate Bni1 into clusters) is redundant with another cellular factor not present in our in vitro assays. Indeed, while Bni1-GFP is less focused in *bil2*Δ cells, there is still some polarization of Bni1-GFP at mating projection tips, suggesting that other factors besides Bil2 contribute to focusing Bni1 at mating projection tips, for example, possibly Spa2, Pea2, Aip5, and Bil1 (Xie and Miao, 2021).

Broad implications for understanding how formins are spatially regulated

Our results provide new insights into how formins are spatially regulated in vivo. During mitotic growth Bnr1 is anchored at the bud neck via its association with septins and septin-associated proteins. However, it has been unclear how Bni1 becomes concentrated at the bud tip during mitotic growth and at the shmoo tip during the mating response. Our results suggest that Bil2 plays an important role in focusing Bni1 at the mating projection tips. Recent studies suggest that Bni1, Bud6, and other polarisome components may undergo phase separation at polarity sites to form molecular condensates (Xie and Miao, 2021). Our observations raise the possibility that Bil2 (15 kDa) is involved in this process. Interestingly, IUPred2a (iupred2a.elte.hu) predicts a short intrinsically disordered region (IDR) in Bil2, which is a signature of proteins that promote weak multivalent interactions and phase separate.

Our findings may serve as a paradigm for understanding how formins are organized in other systems where they are locally concentrated to promote actin assembly, for example, filopodia tips, stereocilia tips, podosomes tips, focal adhesions, cytokinetic nodes, ER-mitochondrial contact sites, pollen tube tips, and the fission yeast "actin fusion focus" (Wu *et al.*, 2006; Yang *et al.*, 2007; Yonetani *et al.*, 2008; Chesarone *et al.*, 2010; Korobova *et al.*, 2013; Dudin *et al.*, 2015; Gauvin *et al.*, 2015; Panzer *et al.*, 2016). Perhaps the closest examples to what we describe here for *S. cerevisiae* Bni1 forming a focused spot at mating projection tips are the concentration of *S. pombe* formin Fus1 at sites where cells of opposite mating type fuse (Dudin *et al.*, 2015) and the concentration of *S. pombe* formin Cdc12 at cytokinetic nodes (Wu *et al.*, 2006; Yonetani *et al.*, 2008). The ability of *S. pombe* Fus1 to be tightly focused at cell fusion sites depends on its large IDR, suggesting that Fus1, alone or together with other factors, phase separates into molecular condensates at these sites (Billault-Chaumartin *et al.*, 2022). The spatial focusing of *S. pombe* Cdc12 into cytokinetic nodes in vivo depends on its binding partner Cdc15 (an F-BAR protein with a large IDR), and Cdc12 and Cdc15 phase separate together in vitro (Willet *et al.*, 2015; Bhattacharjee *et al.*, 2023). The factors that promote spatial focusing of *S. cerevisiae* Bni1 versus *S. pombe* Fus1 and Cdc12 are likely to be different, given that *S. pombe* and *S. cerevisiae* are evolutionarily quite distant from each other (Sipiczki, 2000). Recent studies in *S. cerevisiae* have shown that the polarity proteins Spa2 and Aip5 (which both bind to Bni1) phase separate in vitro and form large condensates in mitotically dividing cells (Xie *et al.*, 2019; Xie and Miao, 2021). We have shown that Bil2, another protein with low complexity, plays an important role in concentrating Bni1 at mating projection tips. Thus, Bil2 may function together with these other polarity proteins to focus Bni1 localization. Altogether, these observations in budding yeast and fission yeast provide three key examples of formins (Bni1, Fus1, and Cdc12) that are spatially focused in vivo to drive the formation of different actin structure (actin cables, actin fusion focus, and cytokinetic actin ring, respectively). These multiple examples suggest that spatial focusing of formins may be important in many other settings, including filopodial tips, focal adhesions, and stereocilia tips.

MATERIALS AND METHODS

Request a protocol through *Bio-protocol*.

Plasmids and yeast strains

For live imaging of secretory vesicles, we transformed yeast with previously described CEN plasmids that express either GFP-*SEC4* or mCherry-*SEC4* (Rands and Goode, 2021). For localizing Bil2 in live cells, we used a previously described low copy (CEN) plasmid expressing N-terminally tagged GFP-Bil2 from a constitutive promoter (Rands and Goode, 2021). For *E. coli* purification of 6His-Bil2, we used a previously described plasmid (Rands and Goode, 2021). For galactose-induced expression and purification of 6xHis-SNAP-Bni1$^{1228–1953}$ (FH1-FH2-C) in *S. cerevisiae*, we used a previously described plasmid (Pollard *et al.*, 2020). For galactose-induced expression and purification of 6xHis-FL-Bni1$^{1–1953}$ (full-length) in *S. cerevisiae,* we introduced the entire open reading frame of Bni1 into the same vector as the plasmid expressing 6xHis-C-Bni1$^{1228–1953}$ (FH1-FH2-C; Moseley and Goode, 2006). For *E. coli* expression of 6xHis-SUMO-Bni1$^{1228–1953}$ (FH1-FH2-C), we used a previously described plasmid (Wirshing *et al.*, 2023). For *E. coli* expression of MBP-Bud6(full-length)-6His, we constructed a new plasmid by PCR amplification of the entire *BUD6* open reading frame (encoding residues 1–788) with a C-terminal 6xHis tag, and cloned this PCR product into the SalI and HindIII sites of the pMAL-c4x plasmid (Walker *et al.*, 2010), which adds an N-terminal MBP tag.

For galactose-induced expression of Bni1 polypeptides in *S. cerevisiae*, we used the protease-deficient yeast strain BJ2168: *MATa leu2 trp1 ura3–52 pep4–3 prc1–407 prb1–1122 gal2* (ATCC 208277) (Jones, 1977). For Supplemental Figure S1, A and B, we used wildtype and *bni1*Δ yeast strains in the Research Genetics S288C background (*MATa*, *ura3*, *leu2*, *his3*, *met15*). All other yeast strains were in the W303 background (*leu2-3,112 trp1-1 can1-100 ura3-1 ade2-1 his3-11,15 [phi+]*). Gene deletions were introduced by homologous recombination (Longtine *et al.*, 1998b) to generate *bni1*Δ and *bnr1*Δ, as well as *bil2*Δ (BGY4248) and *bud6*Δ (BGY1418) strains. Genetic crosses followed by tetrad dissections were performed to generate double mutant strains *bud6*Δ*bil2*Δ (BGY4260) and *bnr1*Δ*bil2*Δ. *BUD6* point mutant strains (*bud6-35* and *bud6-8*) were generated as described (Graziano *et al.*, 2011). Standard PCR-based genome modification methods (Longtine *et al.*, 1998b) were used to tag endogenous Bni1 at its C-terminus with either enhanced GFP (GFP^{ENVY}) of mScarlet, endogenous Bnr1 at its C-terminus with GFP^{ENVY}, endogenous Abp140 at its C-terminus with GFP^{ENVY}, endogenous Tub1 at its C-terminus with GFP^{ENVY}, and endogenous Spc72 at its C-terminus with GFP^{ENVY}. Endogenous Bem1 was C-terminally tagged with yomRuby2 by transforming pRSII405-Bem1-mRuby linearized with SalI (Simke *et al.*, 2022).

Imaging of actin cables in fixed cells

To analyze actin cable organization in vivo, yeast strains were grown in YEPD media to OD_{600} = 0.4–0.6, and then treated for 3 h with 100 µM alpha factor (Zymo research; Irvine CA), fixed in 5% formaldehyde for 20 min at room temperature, and washed three times with PBS buffer. Cells were stained 1–3 d with Alexa Fluor 488 phalloidin (Life Technologies; Grand Island, NY), washed three times with PBS buffer, then imaged. For quantifying cable tortuosity, cells were imaged by structured illumination microscopy (SIM) on a Nikon Ti-2 SIM-E inverted microscope with a Hamamatsu Orca Flash 4.0 camera controlled by NIS-Elements software (Nikon Instruments), using an exposure time of 200 ms at 488 nm excitation and 40% laser power. Actin cables were traced in FIJI software by tracing the cable with the multipoint tool. Cable tortuosity (length/distance)

was determined by measuring total length of the cable (adding together all the distances between points) and dividing it by the distance between the first and last points.

For comparing actin cable network organization (images in Figure 4A), strains were grown to log phase as above, then fixed in 4.4% formaldehyde for 45 min at 25°C. Cells were then washed in 1x PBS (pH 7.3), resuspended in 1x PBS (pH 7.3) + 0.1% Triton X-100, and stained with Alexa Fluor 488-phalloidin (Life Technologies) overnight at 4°C. Then cells were washed in 1x PBS (pH 7.3), resuspended with Vectashield mounting media (Vector Laboratories), mounted on slides, and imaged on a Nikon Ti2-E invert confocal microscope equipped with a CSU-W1 SoRa (Yokogawa) and a Prime BSI sCMOS camera (Teledyne Photometrics) controlled by Nikon NIS-Elements Advanced Research software using a 60x, 1.40 NA objective, using an exposure time of 500 ms at 488 nm excitation and 40% laser power. Three-dimensional stacks through the entire cell were acquired at 0.2 µm steps. Images were denoised using NIS-Elements Advanced Research software (Nikon).

Live cell imaging

For live imaging of mating projection formation, strains were grown in YEPD media at 25°C to OD_{600} = 0.4–0.6, then treated with 100 µM alpha factor for 1 h, and introduced into flow chambers. Flow chambers were constructed by sandwiching glass coverslips (pretreated with 1 mg/ml concanavalin a) on top of plastic flow chambers (Ibidi, Fitchburg, WI) using double-sided tape (2.5 cm 3 × 2 mm 3 × 120 mm) and 5-min epoxy resin (Devcon, Riviera Beach, FL). Cells were imaged on a Nikon Ti-2 SIM-E inverted microscope with a Hamamatsu Orca Flash 4.0 camera controlled by NIS-Elements software (Nikon Instruments) using transmitted light. One image was taken every 5 min for 6 h. Mating projections were also assessed by live imaging at designated time points after exposure to pheromone (Figure 2A; Supplemental Figure S2, A and B), where cells were mounted onto slides and imaged on a Nikon Ti2-E invert confocal microscope equipped with a CSU-W1 SoRa (Yokogawa) and a Prime BSI sCMOS camera (Teledyne Photometrics) controlled by Nikon NIS-Elements Advanced Research software using a 100x, 1.40 NA objective, and the brightfield setting.

For assessing mating projections in S288C and W303 yeast strain backgrounds, cells were grown to mid log-phase in synthetic complete (SC) media and then exposed to 100 µM alpha factor for 3 and 5 h. For latrunculin B experiments in Supplemental Figure S1B, both S288C and W303 yeast cells were grown to mid log-phase in SC media and then exposed to 100 µM alpha-factor and 100 µM latrunculin B for 3 h. Cells were imaged on a Nikon Ti2-E invert confocal microscope equipped with a CSU-W1 SoRa (Yokogawa) and a Prime BSI sCMOS camera (Teledyne Photometrics) controlled by Nikon NIS-Elements Advanced Research software using a 100 × 1.40 NA objective using an exposure time of 300 ms with the brightfield setting.

For quantifying cell circularity, yeast cells were grown to mid log-phase in YPD and treated with 100 µM alpha factor (Zymo Research, Irvine CA) for 3 h and imaged on a Nikon Ti2-E invert confocal microscope equipped with a CSU-W1 SoRa (Yokogawa) and a Prime BSI sCMOS camera (Teledyne Photometrics) controlled by Nikon NIS-Elements Advanced Research software using a 60x, 1.40 NA objective. Images were acquired using 100 ms exposures with the brightfield setting. Cell circularity was quantified by manually tracing cell outlines using the circularity function in FIJI, which uses the equation: $4\pi \bullet (\text{cell area}/\text{cell perimeter}^2)$.

For examining the localization of endogenously tagged Bni1-GFP and Bnr1-GFP and quantifying their cellular abundance (Figure 1, C–F), cells were grown to mid log-phase in SC media and treated with 100 µM alpha factor for 3 h and imaged on a Nikon Ti2-E invert confocal microscope equipped with a CSU-W1 SoRa (Yokogawa) and a Prime BSI sCMOS camera (Teledyne Photometrics) controlled by Nikon NIS-Elements Advanced Research software using a 100x, 1.40 NA objective using an exposure time of 500 ms at 488 nm excitation and 50% laser power. Three-dimensional stacks through the entire cell were acquired at 0.3 µm steps, from which sum projections were generated. To control for autofluorescence background, a parent yeast strain (with no GFP tag) was grown and imaged in parallel using the identical settings. The average mean intensity of the control cells, with and without alpha factor treatment, was calculated (and defined as background), then subtracted from the mean intensities determined for Bni1-GFP and Bnr1-GFP cells. Cell outlines were manually traced and the fluorescence levels for each cell were divided by its cell area (μm^2) in FIJI. For examining Bnr1-GFP localization after pheromone exposure and acutely treated with latrunculin B, cells were grown to mid log-phase in SC media and treated with 100 µM alpha factor for 2.5 h. Following pheromone treatment, cells were treated with either 100 µM latrunculin B or DMSO for 10 min and imaged as described above for Bnr1-GFP.

For live imaging of secretory vesicles, yeast cells were transformed with a CEN plasmid expressing GFP-Sec4, grown in synthetic selective media at 25°C until they reached OD_{600} = 0.4-0.6, and treated with 100 µM alpha factor for the indicated times in figures. Cells were mounted on slides and imaged on an i-E upright confocal microscope (Nikon Instruments) with a CSU-W1 spinning disk head (Yokogawa), 100 × oil objective (NA 1.4; Nikon Instruments), and an Ixon 897 Ultra-CCD camera (Andor Technology) controlled by NIS-Elements software (Nikon Instruments). For the still-shot images shown in Figure 2C, we used exposure times of 200 ms at 50% intensity (excitation 488 nm) to image cells in 21-step Z-stacks (0.3 µm steps). For live imaging of secretory vesicle transport (Figure 4D), we imaged cells in a single focal plane with exposure times of 50 ms at 50% intensity (excitation 488 nm) at 100-ms intervals. Vesicle delivery frequencies were determined by counting the number of GFP-Sec4 puncta translocated from the main body of the cell to within 2.5 µm of the mating projection tip in a 60 s observation window.

For live imaging of Bni1-GFP to examine how well it localizes to mating projection tip (Figure 6, A and B), cells were grown in synthetic selective media at 25°C until they reached OD_{600} = 0.4–0.6, and treated with 100 µM alpha factor for 2.5 h. Cells were then mounted on slides, and imaged using an i-E upright confocal microscope (Nikon Instruments) with a CSU-W1 spinning disk head (Yokogawa), 100 × oil objective (NA 1.4; Nikon Instruments), and an Ixon 897 Ultra-CCD camera (Andor Technology) controlled by NIS-Elements software (Nikon Instruments). Exposure times of 300 ms at 60% intensity (excitation 488 nm) were used to image cells in 17-step Z-stacks (0.3 µm steps). To quantify the fraction of Bni1-GFP signal within 2.5 µm of the mating projection tip, we used ImageJ as follows. Z-stacks were combined using the "sum projection" function, then a region of interest (ROI) was drawn to encompass the mating tip (first 2.5 µm). Fluorescence in the tip region (raw integrated density in FIJI) was measured and divided by total fluorescence in the cell. To compare total Bni1-GFP signals in cells between different strains, we normalized for cell area by taking the total Bni1-GFP signal in each cell (raw integrated density in FIJI) for the same cells as above and dividing this by the cell area (μm^2). For high resolution images of Bni1-GFP in cells (Figure 6A; Supplemental Figure S2, D and E) images were acquired on a Nikon Ti2-E invert confocal microscope equipped with a CSU-W1 SoRa (Yokogawa) and a Prime BSI sCMOS camera (Teledyne Photometrics) controlled by Nikon

NIS-Elements Advanced Research software using a 100 × 1.40 N objective using an exposure time of 500 ms at 488 nm excitation and 50% laser power. Three-dimensional stacks through the entire cell were acquired at 0.3 µm steps. Quantification for Supplemental Figure S2C was performed as described for Figure 6B.

Measuring the distance of the spindle pole body and microtubule bundle from shmoo tip

Strains expressing an integrated spindle pole body marker (Spc72-GFP) or microtubule marker (Tub1-GFP) were grown in SC media at 25°C to OD_{600} ~0.4, then treated with 100 µM alpha factor for 3 h. Cells were mounted on slides and imaged on an i-E upright confocal microscope (Nikon Instruments) with a CSU-W1 spinning disk head (Yokogawa), 100 × oil objective (NA 1.4; Nikon Instruments), and an Ixon 897 Ultra-CCD camera (Andor Technology) controlled by NIS-Elements software (Nikon Instruments). For imaging Spc72-GFP, images were captured with exposure times of 400 ms at 60% intensity (excitation 488 nm) in 17-step Z-stacks. Tub1-GFP was imaged similarly, except that images were captured with exposure times of 100 ms at 40% intensity (excitation 488 nm). Images were analyzed in ImageJ as follows. Sum intensity projections were generated from the Z-stacks and the line tool in FIJI was used to measure the distance from the tip of the mating projection to either the center of the nuclear microtubule bundle (Tub1-GFP) or to the center of the spindle pole body (Spc72-GFP), which was then divided by the total length of the mating cell (from tip to posterior). Images shown for Spc72-GFP and Tub1-GFP (Figure 5, A and C) were obtained on a Nikon Ti2-E invert confocal microscope equipped with a CSU-W1 SoRa (Yokogawa) and a Prime BSI sCMOS camera (Teledyne Photometrics) controlled by Nikon NIS-Elements Advanced Research software using a 60x or 100x, 1.40 NA objective, respectively. Images were acquired using an exposure time of 500 ms at 488 nm excitation and 50% laser power. Three-dimensional stacks through the entire cell were acquired at 0.3 µm steps.

Gradient tracking and microfluidics-coupled imaging

Microfluidic chambers were assembled using Sylgard 184 (Dow) and 24 × 40 mm coverslips as previously described (Suzuki *et al*., 2021). The mold was fabricated by the University of Maine Frontier Institute for Research in Sensor Technologies (FIRST). For all the live cell microfluidic experiments, cultures were grown in sterile filtered SC media to an OD600 between 0.2–0.5 at 30°C. The device was then set up with sterile-filtered SC media with either a gradient of alpha factor (0–150 nM) or a flat concentration (300 nM) of alpha factor and Alexa 647 hydrazide at 62 ng/mL to track flow in the device. Timelapse imaging was performed using an Olympus IX83 epifluorescence microscope with a Prior HLD117 stage and a Prime 95B CMOS Camera (Photometrics) controlled by Cell Sens 1.17 (Olympus) and equipped with an Olympus-APON-60X-TIRF objective with excitation light provided by an X-Cite 120 LEDBoost (Excelitas). Images were captured at 20-min intervals for 12 h while cells were maintained at 30°C using an objective heater (Bioptechs). Images were deconvolved with Huygens software (Scientific Volume Imaging) using a theoretical point-spread function and the classical algorithm with signal to noise ratio of 30 and acuity of –21. Masks were generated using Cellpose 2.0 (Stringer *et al*., 2021) and FIJI (Schindelin *et al*., 2012) while the data analysis was performed using MATLAB (Mathworks). For gradient tracking experiments, polar histograms were obtained from two independent experiments measuring the orientation of each cell in degrees. A line tool in FIJI was used to draw a line from the inside of each cell towards the tip and angles were measured. The data (angles) were then used in MATLAB to generate polar histograms.

To quantify time to establishment of polarity, we exposed cells expressing endogenously tagged Bni1-GFP and Bem1-mRuby to a flat low concentration of alpha factor (100 nM), sufficient to drive elongated cell growth. We then performed time lapse (DIC and fluorescence) imaging to assess establishment of polarity. Use of a flat concentration of pheromone yields a large number of cells that can be analyzed, because every cell experiences the same dose of pheromone. In contrast, in the gradient tracking experiments, only cells in the central third of the chamber experience a dose that drives elongation. We defined the time of stable polarity establishment as the time at which a projection first appeared.

To assess spatial focusing of Bni1-GFP in cells, we used the previously described Granulinator MATLAB (Mathworks) script (https://github.com/Kelley-Lab-Computational-Biology/Granule, [Hunn *et al*., 2022]). Cell masks were generated with Cellpose (Stringer *et al*., 2021), and then the images were analyzed by Granulinator using the following settings: threshold of three standard deviations above the mean, 150 brightest pixels excluded from calculation of the mean and standard deviations, and a minimum spot size of 20 eight-connected pixels.

Protein purification

Rabbit skeletal muscle actin was purified from acetone powder (Spudich and Watt, 1971) generated from frozen ground hind leg muscle tissue of young rabbits (Pel-Freez Biologicals, Rogers, AR). Lyophilized acetone powder stored at –80°C was mechanically sheared in a coffee grinder, resuspended in G-buffer (5 mM Tris-HCl, pH 8.0, 0.2 mM adenosine 5′-triphosphate [ATP], 0.5 mM dithiothreitol [DTT], 0.1 mM $CaCl_2$), and then cleared by centrifugation for 20 min at 50,000 × *g*, 4°C. The supernatant was filtered through Grade 1 Whatman paper, and then actin was polymerized by the addition of 2 mM $MgCl_2$ and 50 mM NaCl to the filtrate and overnight incubation at 4°C with slow stirring. The next morning, NaCl was added to a final concentration of 0.6 M, and stirring was continued for another 30 min at 4°C. F-actin was pelleted by centrifugation for 150 min at 120,000 × *g*, 4°C. The pellet was solubilized by dounce homogenization and dialyzed against 1 l of G-buffer at 4°C (three consecutive times at 12–18 h intervals). Monomeric actin was then precleared for 30 min at 435,000 × *g*, 4°C, and loaded onto a S200 (16/60) gel-filtration column (GE Healthcare, Marlborough, MA) equilibrated in G-buffer. Peak fractions were stored at 4°C.

For the fluorescently labeled actin used in TIRF microscopy assays, actin was labeled on cysteine 374 as previously described (Kuhn and Pollard, 2005). Briefly, the F-actin pellet described above was dounce homogenized and dialyzed against G-buffer lacking DTT. Monomeric actin was then polymerized by adding an equal volume of 2 × labeling buffer (50 mM imidazole, pH 7.5, 200 mM KCl, 0.3 mM ATP, 4 mM $MgCl_2$). After 5 min, the actin was mixed with a five-fold molar excess of Alexa488 maleimide (Thermo Fisher Scientific, Waltham, MA), resuspended in anhydrous dimethylformamide, and incubated in the dark for 15 h at 4°C. Labeled F-actin was pelleted as above, and the pellet was rinsed briefly with G-buffer, then depolymerized by dounce homogenization, and dialyzed against G-buffer for 2 d at 4°C. Labeled, monomeric actin was purified further on a S200 (16/60) gel-filtration column (GE Healthcare) equilibrated in G-buffer. Peak fractions of Alexa488-actin were pooled and dialyzed for 15 h against G-buffer with 50% glycerol and stored at –20°C. The concentration and labeling efficiency were determined by measuring absorbance at 280 and 494 nm. Molar

extinction coefficients: ε_{290} actin = 26,600 M^{-1} cm^{-1}, ε_{494} Alexa488 = 71,000 M^{-1} cm^{-1}, and Alexa488 correction factor at 290 = 0.11.

For preparing biotinylated actin used in TIRF microscopy assays, the F-actin pellet above was dounce homogenized and dialyzed against G-buffer lacking DTT. Monomeric actin was then polymerized by the addition of an equal volume of 2 × labeling buffer. After 5 min, the actin was mixed with a five-fold molar excess of NHS-XX-Biotin (Merck KGaA, Darmstadt, Germany) and incubated for 15 h at 4°C. The F-actin was pelleted as above, and the pellet was rinsed with G-buffer, then dounce homogenized, and dialyzed against G-buffer for 48 h at 4°C. Biotinylated monomeric actin was purified further on an S200 (16/60) gel-filtration column as above. Aliquots of biotin-actin were snap frozen in liquid nitrogen and stored at –80°C.

For bulk pyrene-actin assembly assays, actin was labeled with pyrenyl-iodoacetamide on cysteine 374 (Pollard and Cooper, 1984). Actin prepared as above, excluding the gel filtration step, was dialyzed against pyrene buffer (25 mM Tris-HCl, pH 7.5, 100 mM KCl, 0.02% NaN3, 0.3 mM ATP, and 2 mM MgSO4) for 3 h, then diluted with pyrene buffer to 1 mg/ml (23.8 µM). A sevenfold molar excess of pyrenyl-iodoacetamide was added, and this actin solution was incubated overnight at 4°C. Next, aggregates were cleared by low-speed centrifugation, and the supernatant (containing F-actin) was centrifuged for 3 h at 45,000 rpm in a rotor (Ti70; Beckman Coulter) at 4°C to pellet F-actin. The F-actin pellets were mechanically disrupted using a dounce, then dialyzed against G buffer for 1–2 d, and finally gel filtered on a 16/60 S200 column as above. Peak fractions were pooled, aliquoted, snap frozen, and stored at –80°C until use.

6xHis-SNAP-Bni1$^{1228–1953}$ was expressed by galactose-induction from a plasmid transformed into the protease-deficient yeast strain BJ2168, essentially as described (Moseley *et al*., 2006). Cells were grown to OD_{600} = 0.8 in 2 l SC media (lacking uracil) with 2% raffinose, then expression was induced by shifting cells to the same media with 2% galactose and adding 20 g bacto-peptone and 10 g yeast extract (US Biologicals, Salem, MA). After overnight induction at 25°C, yeast cells were harvested by centrifugation at 4°C at 5000 × g for 20 min, washed with water, resuspended in 0.2 vol water, and flash frozen as pellets in liquid N2. Mechanical lysis was performed using a coffee grinder to pulverize yeast into a fine powder while submerged in liquid N2. The yeast powder was resuspended and thawed in lysis buffer A (300 mM NaCl and 50 mM NaPO4, pH 8.0), transferred to ice, and supplemented with 1 × protease inhibitors and 0.5 mM DTT. Lysates were clarified two times to remove cellular debris by sequential centrifugation steps at 4°C, first at 28,000 × g for 15 min, and then at 310,000 × g for 30 min. The high-speed supernatant (~20 ml) was then incubated with 0.5 ml Ni2+-NTA-agarose resin (Qiagen, Valencia, CA), rotating at 4°C for 1 h. The resin was washed with 100 ml of high salt wash buffer (20 mM imidazole, pH 8.0, 20 mM NaPO4, pH 8.0, 0.5 mM DTT, and 500 mM NaCl) and then 100 ml of low salt wash buffer (same as above, but with 150 mM NaCl). The protein was eluted from the beads with elution buffer (150 mM NaCl, 250 mM imidazole, pH 8.0, 20 mM NaPO4, pH 8.0, and 1 mM DTT). The buffer was exchanged to SNAP-labeling buffer (150 mM NaCl, 20 mM NaPO4, pH 8.0, and 1 mM DTT) using a PD-10 desalting column (GE Healthcare), and the protein was concentrated by Amicon-Ultra filtration (EMD Millipore). The 6xHis-SNAP-Bni1$^{1228–1953}$ protein was then mixed with a 2–3 M excess of biotin-Alexa549-benzylguanine (New England Biolabs, Ipswich, MA) for 18 h at 4°C, rotating in the dark. To remove excess dye, buffer was exchanged into $HEKG_{10}$ buffer using a 0.5 ml Zeba spin desalting column (Thermo Fisher), and aliquots were snap frozen in liquid N2 and stored at –80°C. Labeling efficiency was 95–100%. Protein concentration was determined by Bradford (using a bovine serum albumin [BSA] standard) and labeling efficiency was determined by absorbance using extinction coefficients: ε280 = 66,810 M–1cm–1 for the protein, and ε560 = 150,000 M–1cm–1 for the Alexa549, with a ε280 correction factor of 0.08 for the dye.

6His-FL-Bni1$^{1–1953}$ and 6His-C-Bni1$^{1228–1953}$ polypeptides were expressed in *S. cerevisiae* strain BJ2168 by galactose-induction as described (Moseley *et al*., 2006). For each purification, 2 l of yeast cells in synthetic medium lacking uracil with 2% raffinose were grown to OD_{600} = 0.6–0.9. Then expression was induced by addition of dry ingredients: 10 g yeast extract, 20 g peptone, and galactose (2% wt/vol). Cells were grown for 12–16 h at 30°C, then pelleted, washed in H_2O, frozen dropwise in liquid N_2, and stored at –80°C. To initiate a protein preparation, frozen yeast pellets were lysed mechanically in a coffee grinder cooled with liquid N_2. Then, 20 g of lysed yeast powder was resuspended in 20 ml of buffer A (20 mM $NaPO_4$, pH 7.4, 150 mM NaCl, 30 mM imidazole, 0.5 mM DTT, 1% NP-40) supplemented with protease inhibitor cocktail (1 mM phenylmethylsulfonyl fluoride, 0.5 µM each of pepstatin A, antipain, leupeptin, aprotinin, and chymostatin), and cleared by ultracentrifugation at 200,000 × *g* for 20 min in a TLA100.3 rotor (Beckman Coulter). Cleared lysates were then passed through a 0.45-µm syringe filter (Millex, MilliporeSigma; Darmstadt, Germany), mixed with 2 ml of Ni-NTA beads (New England Biolabs; Ipswich, MA), and incubated for 1 h at 4°C with gentle agitation. Beads were washed three times with 10 ml wash buffer (20 mM Tris pH 8.0, 500 mM NaCl, 0.5 mM DTT, 30 mM Imidazole), and 6His-Bni1 was eluted with 4 ml of elution buffer (20 mM Tris pH 8.0, 500 mM NaCl, 0.5 mM DTT, 300 mM Imidazole). Peak fractions were pooled and loaded on a PD10 desalting column (GE Life Sciences; Marlborough, MA) equilibrated in $HEKG_{10}D$ buffer (20 mM HEPES, pH 7.5, 1 mM EDTA, 50 mM KCl, 10% [vol/vol] glycerol, and 1 mM DTT), then concentrated to ~200 µl, aliquoted and snap frozen in liquid N_2, and stored at –80°C.

C-Bni1$^{1228–1953}$ (no tag) was also purified as follows. 6xHis-SUMO-Bni1$^{1227–1953}$ was expressed in *E. coli* strain Rosetta (DE3) with the pRARE rare codon plasmid (MilliporeSigma; Darmstadt, Germany). Cells were grown to log phase in Terrific Broth at 37°C and induced with 1 mM IPTG (Isopropyl β-D-1-thiogalactopyranoside) for 16 h at 18°C. Cells were harvested by centrifugation and pellets were stored at –80°C. Pellets were resuspended in lysis buffer (30 mM imidazole, pH 8.0, 0.5 mM DTT, and 2 × PBS [40 mM sodium phosphate buffer and 200 mM NaCl, pH 7.4]) supplemented with 150 mM NaCl, 1% NP-40, and protease inhibitors. Next, cells were lysed using a probe sonicator on ice, clarified by centrifugation at 27,000 × g for 30 min at 4°C, and mixed with 1 ml nickel–nitrilotriacetic acid (Ni-NTA)–agarose beads (Qiagen) for 1 h at 4°C. The slurry was transferred to an empty column, and the agarose was allowed to settle by gravity. The column was washed twice with 10 column volumes of lysis buffer plus 350 mM NaCl, and then twice with 10 column volumes of wash buffer (20 mM HEPES pH 7.5, 100 mM NaCl, 5% glycerol). C-Bni1$^{1228–1953}$ was then eluted using wash buffer plus 250 mM imidazole. The 6xHIS-SUMO tag was removed from the formins by overnight digestion at 4°C with Ulp1 protease, while dialyzing the reaction against 500 ml $HEKG_5$ buffer (20 mM HEPES pH 7.5, 1 mM EDTA, 50 mM KCl, 10% glycerol) with 2 mM DTT. Following dialysis, Bni1 FH1-C was further purified by gel filtration on a Sup6 column (GE Healthcare) equilibrated in buffer $HEKG_{10}$ with 1 mM DTT using an AKTA FPLC (GE Healthcare). Peak fractions were pooled, concentrated, aliquoted, snap frozen, and stored at –80°C.

S. cerevisiae profilin was expressed in BL21(DE3) *E. coli* and purified as described (Graziano *et al*., 2013). Bacterial cells were grown in terrific broth to log phase and induced with 0.4 mM IPTG for

3–4 h at 37°C. Cells were pelleted and stored at –80°C. Frozen pellets were thawed, resuspended in lysis buffer (20 mM Tris-HCl, pH 8.0) supplemented with protease inhibitor cocktail, and lysed by incubation with lysozyme and sonication. Lysates were cleared by centrifugation at 200,000 × *g* at 4°C for 20 min in a TLA-100.3 rotor (Beckman Coulter). The supernatant was then loaded on a 5 ml HiTrap Q fast flow column (GE Healthcare), and profilin was eluted using a 75 ml salt gradient (0–400 mM NaCl) in 20 mM Tris-HCl, pH 8.0. Peak fractions were pooled, concentrated to 5 ml, and loaded on a Superdex 75 (26/60) gel filtration column (GE Healthcare) equilibrated in G-buffer. Peak fractions were pooled and exchanged into $HEKG_{10}D$ buffer on a PD10 desalting column as above, and aliquots were snap frozen in liquid N_2 and stored at –80°C.

6His-Bil2 was expressed in Rosetta 2 BL21(DE3) *E. coli* cells carrying with the pRARE rare codon plasmid. Cells were grown to OD_{600} = 0.7–0.9 in terrific broth supplemented with kanamycin and chloramphenicol to maintain selection of the expression plasmid and the pRARE plasmid, respectively. Expression was induced with 0.4 mM IPTG overnight at 18°C, and then cells were pelleted and stored at –80°C. To initiate a preparation, a cell pellet was thawed, resuspended in lysis buffer (20 mM Tris pH 8.0, 500 mM NaCl, 0.5 mM DTT, 30 mM Imidazole) supplemented with protease inhibitor cocktail, and lysed by treatment with 1 mg/ml lysozyme, 0.1 mg/ml DNAse I, and sonication. Lysates were cleared by centrifugation at 10,000 × *g* for 20 min in an F21S-8 × 50y rotor (Thermo Fisher Scientific; Waltham, MA), and the supernatant was mixed with 1 ml of Ni-NTA beads (New England Biolabs) and rotated at 4°C for 1 h. The beads were then washed three times with 10 ml wash buffer (20 mM Tris pH 8.0, 500 mM NaCl, 0.5 mM DTT, 30 mM Imidazole) in a gravity column at 4°C. 6His-Bil2 was eluted from the beads using elution buffer (20 mM Tris pH 8.0, 500 mM NaCl, 0.5 mM DTT, 300 mM Imidazole), then exchanged into $HEKG_{10}D$ buffer on a PD10 desalting column (GE Life Sciences), concentrated to ~200 µl, and aliquots were snap frozen in liquid N_2 and stored at –80°C.

Full-length MBP-Bud6-6His was expressed in Rosetta 2 BL21(DE3) *E. coli* cells carrying the pRARE rare codon plasmid. Cells were grown to OD_{600} = 0.7–0.9 in terrific broth supplemented with 0.2% glucose, as well as ampicillin and chloramphenicol to maintain selection of the expression plasmid and the pRARE plasmid, respectively. Expression was induced with 0.4 mM IPTG overnight at 18°C, and then cells were pelleted and stored at –80°C. Cell pellets were thawed, resuspended in lysis buffer (20 mM Tris pH 8.0, 200 mM NaCl, 1 mM DTT, 1 mM EDTA) with protease inhibitor cocktail, and lysed as above for 6His-Bil2. Lysates were cleared by centrifugation at 10,000 × *g* for 20 min in an F21S-8 × 50y rotor (Thermo Fisher Scientific), and the supernatant was mixed with 1 ml of amylose beads (New England Biolabs), and incubated for 1 h at 4°C rotating. The beads were then washed three times with 10 ml wash buffer (20 mM Tris pH 8.0, 200 mM NaCl, 1 mM DTT, 1 mM EDTA) in a gravity column at 4°C. MBP-Bud6-6His was eluted from the beads using MBP elution buffer (20 mM Tris pH 8.0, 200 mM NaCl, 1 mM DTT, 20 mM Maltose) and collected in 0.5 ml fractions. Peak fractions were pooled, mixed with 1 ml of Ni-NTA beads (New England Biolabs) and rotated at 4°C for 1 h. The beads were then washed three times with 10 ml wash buffer (20 mM Tris pH 8.0, 500 mM NaCl, 0.5 mM DTT, 30 mM Imidazole) in a gravity column at 4°C. MBP-Bud6-6His was eluted from the beads using elution buffer (20 mM Tris pH 8.0, 500 mM NaCl, 0.5 mM DTT, 300 mM Imidazole), then exchanged into $HEKG_{10}D$ buffer on a PD10 desalting column (GE Life Sciences), concentrated to ~200 µl, and aliquots were snap frozen in liquid N_2 and stored at –80°C.

Pyrene-actin assembly assays

Gel-filtered monomeric muscle actin in G-buffer was cleared by ultracentrifugation for 1 h at 4°C at 350,000 × g in a TLA-100 rotor (Beckman Coulter). The upper ~70% of the supernatant was carefully recovered and used for assembly assays. All reactions (60 µl) contained 2 µM G-actin (5% pyrene-labeled), which was converted to Mg2+-ATP-actin 2 min before use. Then, 42 µl of Mg2+-ATP-G-actin was mixed rapidly with 15 µl of proteins or control buffer and 3 µl of 20 × initiation mix (40 mM $MgCl_2$, 10 mM ATP, 1 M KCl) to initiate polymerization. Fluorescence was monitored at excitation 365 nm and emission 407 nm at 25°C for 1000–2000 s in a fluorimeter (Photon Technology International, Lawrenceville, NJ).

TIRF microscopy

Glass coverslips (60 × 3 × 24 mm; Thermo Fisher Scientific) were cleaned by sonication for 30 min in detergent, followed by 1 M potassium hydroxide (KOH), and 1 M HCl, and then stored in 100% ethanol. Coverslips were coated with a mixture of 4 mg/ml polyethylene glycol (PEG)-silane and 80 mg/ml biotin-PEG in 80% ethanol pH 1.0, then washed with water and dried with compressed N2. PEG-coated coverslips were stored for 1–3 d at 70°C before use. Flow chambers were constructed by sandwiching glass coverslips on top of plastic flow chambers (Ibidi, Fitchburg, WI) using double-sided tape (2.5 cm 3 × 2 mm 3 × 120 mm) and five-minute epoxy resin (Devcon, Riviera Beach, FL). To anchor actin filaments in TIRF reactions, 4 mg/ml streptavidin in HEK buffer (20 mM HEPES pH 7.4, 1 mM EDTA, 50 mM KCl) was flowed into the TIRF chamber for 15 s using a syringe pump (Harvard Apparatus, Holliston, MA). Then the chamber was washed with HEK buffer + 1% BSA. The chamber was then equilibrated with TIRF buffer (10 mM HEPES pH 7.4, 50 mM KCl, 1 mM MgCl2, 1 mM EGTA, 0.2 mM ATP, 10 mM DTT, 15 mM glucose, 20 mg/ml catalase, 100 mg/ml glucose oxidase, 10 mM Imidazole, and 0.5% methylcellulose [4000 cP]). Proteins were rapidly mixed with a final concentration of 1 µM G-actin (10% labeled) in 50 µl reactions, and then flowed into the TIRF chamber, which was then immediately mounted on the microscope for imaging. Time-lapse TIRF imaging was performed on a Ti200 inverted microscope (Nikon Instruments, New York, NY) equipped with 100 mW solid-state lasers (Agilent Technologies, Santa Clara, CA), a CFI Apo 60 × 1.49 N.A. oil-immersion TIRF objective (Nikon Instruments), a iXon EMCCD camera with a pixel size of 0.267 mm (Andor Technology), and an additional 1.5 × zoom module (Nikon Instruments). Focus was maintained using the Perfect Focus System (Nikon Instruments). Frames were captured every 10 s for 600 s, with 10 ms exposures (488 nm excitation, 15% laser power) using NIS Elements software (Nikon Instruments). Image analysis was performed in ImageJ, where background fluorescence was removed from each time series using the background subtraction tool in Fiji (rolling ball radius, 50 pixels). For measuring number of actin filaments nucleated in TIRF reactions, fields of view (FOVs) were analyzed 200 s after initiation of TIRF reactions. For each reaction, four separate FOVs were analyzed. To calculate the fraction of filaments nucleated from asters, the number of filaments extending from asters was divided by the total number of filaments in the FOV. Filament elongation rates were determined from $n = 30$ filaments. Filament length was measured using the freehand line tool in ImageJ. Elongation rates were determined by plotting filament length versus time, where the rate is the slope. To express rates in actin subunits s^{-1}, we used the conversion factor of 374 subunits per µm of F-actin.

ACKNOWLEDGMENTS

We are grateful to members of the Goode lab for creative input on experimental design and models. We are also grateful to James Moseley, Sankar Maiti, and Chris Gould for early work in characterizing purified FL-Bni1. This work was funded by a grant from NIGMS to B.L.G. (R35 GM134895), a grant from NIGMS to J.B.K. (R15 GM140409), and an NRSA postdoctoral fellowship from NIGMS to J.M. (F32 GM150204).

REFERENCES

A M, Fung TS, Kettenbach AN, Chakrabarti R, Higgs HN (2019). A complex containing lysine-acetylated actin inhibits the formin INF2. Nat Cell Biol 21, 592–602.

Alvaro CG, Thorner J (2016). Heterotrimeric G protein-coupled receptor signaling in yeast mating pheromone response. J Biol Chem 291, 7788–7795.

Bhattacharjee R, Hall AR, Mangione MC, Igarashi MG, Roberts-Galbraith RH, Chen J-S, Vavylonis D, Gould KL (2023). Multiple polarity kinases inhibit phase separation of F-BAR protein Cdc15 and antagonize cytokinetic ring assembly in fission yeast. Elife 12, e83062.

Bidlingmaier S, Snyder M (2004). Regulation of polarized growth initiation and termination cycles by the polarisome and Cdc42 regulators. J Cell Biol 164, 207–218.

Billault-Chaumartin I, Muriel O, Michon L, Martin SG (2022). Condensation of the fusion focus by the intrinsically disordered region of the formin Fus1 is essential for cell-cell fusion. Curr Biol 32, 4752–4761.e10.

Bücking-Throm E, Duntze W, Hartwell LH, Manney TR (1973). Reversible arrest of haploid yeast cells in the initiation of DNA synthesis by a diffusible sex factor. Exp Cell Res 76, 99–110.

Buttery SM, Yoshida S, Pellman D (2007). Yeast formins Bni1 and Bnr1 utilize different modes of cortical interaction during the assembly of actin cables. Mol Biol Cell 18, 1826–1838.

Buttery SM, Kono K, Stokasimov E, Pellman D (2012). Regulation of the formin Bnr1 by septins anda MARK/Par1-family septin-associated kinase. Mol Biol Cell 23, 4041–4053.

Chesarone MA, DuPage AG, Goode BL (2010). Unleashing formins to remodel the actin and microtubule cytoskeletons. Nat Rev Mol Cell Biol 11, 62–74.

Chiou J, Balasubramanian MK, Lew DJ (2017). Cell polarity in yeast. Annu Rev Cell Dev Biol 33, 77–101.

Clay L, Caudron F, Denoth-Lippuner A, Boettcher B, Buvelot Frei S, Snapp EL, Barral Y (2014). A sphingolipid-dependent diffusion barrier confines ER stress to the yeast mother cell. Elife 3, e01883.

Drubin DG, Nelson WJ (1996). Origins of cell polarity. Cell 84, 335–344.

Dudin O, Bendezú FO, Groux R, Laroche T, Seitz A, Martin SG (2015). A formin-nucleated actin aster concentrates cell wall hydrolases for cell fusion in fission yeast. J Cell Biol 208, 897–911.

Dyer JM, Savage NS, Jin M, Zyla TR, Elston TC, Lew DJ (2013). Tracking shallow chemical gradients by actin-driven wandering of the polarization site. Curr Biol 23, 32–41.

Errede B, Vered L, Ford E, Pena MI, Elston TC (2015). Pheromone-induced morphogenesis and gradient tracking are dependent on the MAPK Fus3 binding to Gα. Mol Biol Cell 26, 3343–3358.

Eskin JA, Rankova A, Johnston AB, Alioto SL, Goode BL (2016). Common formin-regulating sequences in Smy1 and Bud14 are required for the control of actin cable assembly in vivo. MBoC 27, 828–837.

Evangelista M, Blundell K, Longtine MS, Chow CJ, Adames N, Pringle JR, Peter M, Boone C (1997). Bni1p, a yeast formin linking Cdc42p and the actin cytoskeleton during polarized morphogenesis. Science 276, 118-122.

Evangelista M, Pruyne D, Amberg DC, Boone C, Bretscher A (2002). Formins direct Arp2/3-independent actin filament assembly to polarize cell growth in yeast. Nat Cell Biol 4, 32–41.

Gao L, Bretscher A (2009). Polarized growth in budding yeast in the absence of a localized formin. Mol Biol Cell 20, 2540–2548.

Gao L, Liu W, Bretscher A (2010). The yeast formin Bnr1p has two localization regions that show spatially and temporally distinct association with septin structures. Mol Biol Cell 21, 1253–1262.

Garabedian MV, Stanishneva-Konovalova T, Lou C, Rands TJ, Pollard LW, Sokolova OS, Goode BL (2018). Integrated control of formin-mediated actin assembly by a stationary inhibitor and a mobile activator. J Cell Biol 217, 3512–3530.

Garabedian MV, Wirshing A, Vakhrusheva A, Turegun B, Sokolova OS, Goode BL (2020). A septin-Hof1 scaffold at the yeast bud neck binds and organizes actin cables. Mol Biol Cell 31, 1988–2001.

Gauvin TJ, Young LE, Higgs HN (2015). The formin FMNL3 assembles plasma membrane protrusions that participate in cell-cell adhesion. Mol Biol Cell 26, 467–477.

Ghose D, Elston T, Lew D (2022). Orientation of cell polarity by chemical gradients. Annu Rev Biophys 51, 431–451.

Graziano BR, Grace A, Michelot A, Breitsprecher D, Chang F (2011). Mechanism and cellular function of Bud6 as an actin nucleation – Promoting factor. Mol Biol Cell 22, 4016–4028.

Graziano BR, Jonasson EM, Pullen JG, Gould CJ, Goode BL (2013). Ligand-induced activation of a formin-NPF pair leads to collaborative actin nucleation. J Cell Biol. 201, 595–611.

Haase SB, Reed SI (1999). Evidence that a free-running oscillator drives G1 events in the budding yeast cell cycle. Nature 401, 394–397.

Hasek J, Rupes I, Svobodová J, Streiblová E (1987). Tubulin and actin topology during zygote formation of Saccharomyces cerevisiae. J Gen Microbiol 133, 3355–3363.

Hegemann B, Unger M, Lee SS, Stoffel-Studer I, van den Heuvel J, Pelet S, Koeppl H, Peter M (2015). A cellular system for spatial signal decoding in chemical gradients. Dev Cell 35, 458–470.

Hilioti Z, Sabbagh W, Paliwal S, Bergmann A, Goncalves MD, Bardwell L, Levchenko A (2008). Oscillatory phosphorylation of yeast Fus3 MAP kinase controls periodic gene expression and morphogenesis. Curr Biol 18, 1700–1706.

Hunn JC, Hutchinson KM, Kelley JB, Reines D (2022). Variable penetrance of Nab3 granule accumulation quantified by a new tool for high-throughput single-cell granule analysis. Curr Genet 68, 467–480.

Imamura H, Tanaka K, Hihara T, Umikawa M, Kamei T, Takahashi K, Sasaki T, Takai Y (1997). Bni1p and Bnr1p: downstream targets of the Rho family small G-proteins which interact with profilin and regulate actin cytoskeleton in Saccharomyces cerevisiae. EMBO J 16, 2745–2755.

Jones EW (1977). Proteinase mutants of Saccharomyces cerevisiae. Genetics 85, 23–33.

Jose M, Tollis S, Nair D, Sibarita J-B, McCusker D (2013). Robust polarity establishment occurs via an endocytosis-based cortical corralling mechanism. J Cell Biol 200, 407–418.

Jose M, Tollis S, Nair D, Mitteau R, Velours C, Massoni-Laporte A, Royou A, Sibarita J-B, McCusker D (2015). A quantitative imaging-based screen reveals the exocyst as a network hub connecting endocytosis and exocytosis. Mol Biol Cell 26, 2519–2534.

Juanes MA, Piatti S (2016). The final cut: Cell polarity meets cytokinesis at the bud neck in S. cerevisiae. Cell Mol Life Sci 73, 3115–3136.

Kelley JB, Dixit G, Sheetz JB, Venkatapurapu SP, Elston TC, Dohlman HG (2015). RGS proteins and septins cooperate to promote chemotropism by regulating polar cap mobility. Curr Biol 25, 275–285.

Kono K, Saeki Y, Yoshida S, Tanaka K, Pellman D (2012). Proteasomal degradation resolves competition between cell polarization and cellular wound healing. Cell 150, 151–164.

Korobova F, Ramabhadran V, Higgs HN (2013). An actin-dependent step in mitochondrial fission mediated by the ER-associated formin INF2. Science 339, 464–467.

Kovar DR (2006). Molecular details of formin-mediated actin assembly. Curr Opin Cell Biol 18, 11–17.

Kuhn JR, Pollard TD (2005). Real-time measurements of actin filament polymerization by total internal reflection fluorescence microscopy. Biophys J 88, 1387–1402.

Lawson MJ, Drawert B, Petzold L, Yi T-M (2022). A positive feedback loop involving the Spa2 SHD domain contributes to focal polarization. PLoS One 17, e0263347.

Li F, Higgs HN (2003). The mouse Formin mDia1 is a potent actin nucleation factor regulated by autoinhibition. Curr Biol 13, 1335–1340.

Li F, Higgs HN (2005). Dissecting requirements for auto-inhibition of actin nucleation by the formin, mDia1. J Biol Chem 280, 6986–6992.

Longtine MS, Fares H, Pringle JR (1998a). Role of the yeast Gin4p protein kinase in septin assembly and the relationship between septin assembly and septin function. J Cell Biol 143, 719–736.

Longtine MS, Kenzie AM, Demarini DJ, Shah NG (1998b). Additional modules for versatile and economical PCR-based gene deletion and modification in *Saccharomyces cerevisiae*. Yeast 961, 953–961.

Manatschal C, Farcas A-M, Degen MS, Bayer M, Kumar A, Landgraf C, Volkmer R, Barral Y, Steinmetz MO (2016). Molecular basis of Kar9-Bim1 complex function during mating and spindle positioning. Mol Biol Cell 27, 3729–3745.

Martin SG, Rincón SA, Basu R, Pérez P, Chang F (2007). Regulation of the formin for3p by cdc42p and bud6p. Mol Biol Cell 18, 4155–4167.

Matheos D, Metodiev M, Muller E, Stone D, Rose MD (2004). Pheromone-induced polarization is dependent on the Fus3p MAPK acting through the formin Bni1p. J Cell Biol 165, 99–109.
McClure AW, Minakova M, Dyer JM, Zyla TR, Elston TC, Lew DJ (2015). Role of polarized g protein signaling in tracking pheromone gradients. Dev Cell 35, 471–482.
Merlini L, Dudin O, Martin SG (2013). Mate and fuse: How yeast cells do it. Open Biol 3, 130008.
Miller RK, Matheos D, Rose MD (1999). The cortical localization of the microtubule orientation protein, Kar9p, is dependent upon actin and proteins required for polarization. J Cell Biol 144, 963–975.
Moore TI, Chou C-S, Nie Q, Jeon NL, Yi T-M (2008). Robust spatial sensing of mating pheromone gradients by yeast cells. PLoS One 3, e3865.
Moseley JB, Goode BL (2005). Differential Activities and Regulation of Saccharomyces cerevisiae Formin Proteins Bni1 and Bnr1 by Bud6 *. 280, 28023–28033.
Moseley JB, Goode BL (2006). The Yeast actin cytoskeleton: From cellular function to biochemical mechanism. Microbiol Mol Biol Rev 70, 605 LP–645.
Moseley JB, Maiti S, Goode BL (2006). Formin proteins: purification and measurement of effects on actin assembly. Methods Enzymol 406, 215–234.
Moseley JB, Sagot I, Manning AL, Xu Y, Eck MJ, Pellman D, Goode BL (2004). A conserved mechanism for Bni1- and mDia1-induced actin assembly and dual regulation of Bni1 by Bud6 and profilin. Mol Biol Cell 15, 896–907.
Orlando DA, Lin CY, Bernard A, Wang JY, Socolar JES, Iversen ES, Hartemink AJ, Haase SB (2008). Global control of cell-cycle transcription by coupled CDK and network oscillators. Nature 453, 944–947.
Ozaki-Kuroda K, Yamamoto Y, Nohara H, Kinoshita M, Fujiwara T, Irie K, Takai Y (2001). Dynamic localization and function of Bni1p at the sites of directed growth in Saccharomyces cerevisiae. Mol Cell Biol 21, 827–839.
Palmer RE, Sullivan DS, Huffaker T, Koshland D (1992). Role of astral microtubules and actin in spindle orientation and migration in the budding yeast, Saccharomyces cerevisiae. J Cell Biol 119, 583–593.
Panzer L, Trübe L, Klose M, Joosten B, Slotman J, Cambi A, Linder S (2016). The formins FHOD1 and INF2 regulate inter- and intra-structural contractility of podosomes. J Cell Sci 129, 298–313.
Park E, Graziano BR, Zheng W, Garabedian M, Goode BL, Eck MJ (2015). Structure of a Bud6/Actin Complex Reveals a Novel WH2-like Actin Monomer Recruitment Motif. Structure (London, England : 1993) 23, 1492–1499.
Pollard LW, Garabedian MV, Alioto SL, Shekhar S, Goode BL (2020). Genetically inspired in vitro reconstitution of Saccharomyces cerevisiae actin cables from seven purified proteins. Mol Biol Cell 31, 335–347.
Pollard TD, Cooper JA (1984). Quantitative analysis of the effect of Acanthamoeba profilin on actin filament nucleation and elongation. Biochemistry 23, 6631–6641.
Pruyne D, Evangelista M, Yang C, Bi E, Zigmond S, Bretscher A, Boone C (2002). Role of formins in actin assembly: nucleation and barbed-end association. Science 297, 612–615.
Pruyne D, Gao L, Bi E, Bretscher A (2004). Stable and dynamic axes of polarity use distinct formin isoforms in budding yeast. Mol Biol Cell 15, 4971–4989.
Rands TJ, Goode BL (2021). Bil2 is a novel inhibitor of the yeast formin Bnr1 required for proper actin cable organization and polarized secretion. Front Cell Dev Biol 9, 634587.
Read EB, Okamura HH, Drubin DG (1992). Actin- and tubulin-dependent functions during Saccharomyces cerevisiae mating projection formation. Mol Biol Cell 3, 429–444.
Rose MD (1996). Nuclear fusion in the yeast *Saccharomyces cerevisiae*. Annu Rev Cell Dev Biol 12, 663–695.
Rose MD, Fink GR (1987). KAR1, a gene required for function of both intranuclear and extranuclear microtubules in yeast. Cell 48, 1047–1060.
Sagot I, Klee SK, Pellman D (2002a). Yeast formins regulate cell polarity by controlling the assembly of actin cables. Nat Cell Biol 4, 42–50.
Sagot I, Rodal AA, Moseley J, Goode BL, Pellman D (2002b). An actin nucleation mechanism mediated by Bni1 and profilin. Nat Cell Biol 4, 626–631.
Schindelin J, Arganda-Carreras I, Frise E, Kaynig V, Longair M, Pietzsch T, Preibisch S, Rueden C, Saalfeld S, Schmid B, *et al*. (2012). Fiji: An open-source platform for biological-image analysis. Nat Methods 9, 676–682.
Simke WC, Johnson CP, Hart AJ, Mayhue S, Craig PL, Sojka S, Kelley JB (2022). Phosphorylation of RGS regulates MAP kinase localization and promotes completion of cytokinesis. Life Sci Alliance 5, e202101245.
Sipiczki M (2000). Where does fission yeast sit on the tree of life? Genome Biol 1, REVIEWS1011.
Slubowski CJ, Funk AD, Roesner JM, Paulissen SM, Huang LS (2015). Plasmids for C-terminal tagging in *Saccharomyces cerevisiae* that contain improved GFP proteins, Envy and Ivy. Yeast 32, 379–387.
Spudich JA, Watt S (1971). The regulation of rabbit skeletal muscle contraction. I. Biochemical studies of the interaction of the tropomyosin-troponin complex with actin and the proteolytic fragments of myosin. J Biol Chem 246, 4866–4871.
Stringer C, Wang T, Michaelos M, Pachitariu M (2021). Cellpose: A generalist algorithm for cellular segmentation. Nat Methods 18, 100–106.
Suzuki SK, Kelley JB, Elston TC, Dohlman HG (2021). Gradient tracking by yeast GPCRs in a microfluidics chamber. Methods Mol Biol 2268, 275–287.
Ten Hoopen R, Cepeda-García C, Fernández-Arruti R, Juanes MA, Delgehyr N, Segal M (2012). Mechanism for astral microtubule capture by cortical Bud6p priming spindle polarity in *S. cerevisiae*. Curr Biol 22, 1075–1083.
Tu D, Graziano BR, Park E, Zheng W, Li Y, Goode BL, Eck MJ (2012). Structure of the formin-interaction domain of the actin nucleation-promoting factor Bud6. Proc Natl Acad Sci USA 109, E3424–E3433.
Walker IH, Hsieh P, Riggs PD (2010). Mutations in maltose-binding protein that alter affinity and solubility properties. Appl Microbiol Biotechnol 88, 187–197.
Wang X, Tian W, Banh BT, Statler B-M, Liang J, Stone DE (2019). Mating yeast cells use an intrinsic polarity site to assemble a pheromone-gradient tracking machine. J Cell Biol 218, 3730–3752.
Willet AH, McDonald NA, Bohnert KA, Baird MA, Allen JR, Davidson MW, Gould KL (2015). The F-BAR Cdc15 promotes contractile ring formation through the direct recruitment of the formin Cdc12. J Cell Biol 208, 391–399.
Wirshing ACE, Rodriguez SG, Goode BL (2023). Evolutionary tuning of barbed end competition allows simultaneous construction of architecturally distinct actin structures. J Cell Biol 222, e202209105.
Wu J-Q, Sirotkin V, Kovar DR, Lord M, Beltzner CC, Kuhn JR, Pollard TD (2006). Assembly of the cytokinetic contractile ring from a broad band of nodes in fission yeast. J Cell Biol 174, 391–402.
Xie Y, Miao Y (2021). Polarisome assembly mediates actin remodeling during polarized yeast and fungal growth. J Cell Sci 134, jcs247916.
Xie Y, Sun J, Han X, Turšić-Wunder A, Toh JDW, Hong W, Gao Y-G, Miao Y (2019). Polarisome scaffolder Spa2-mediated macromolecular condensation of Aip5 for actin polymerization. Nat Commun 10, 5078.
Yang C, Czech L, Gerboth S, Kojima S, Scita G, Svitkina T (2007). Novel roles of formin mDia2 in lamellipodia and filopodia formation in motile cells. PLoS Biol 5, e317.
Yonetani A, Lustig RJ, Moseley JB, Takeda T, Goode BL, Chang F (2008). Regulation and targeting of the fission yeast formin cdc12p in cytokinesis. Mol Biol Cell 19, 2208–2219.
Yu JH, Crevenna AH, Bettenbühl M, Freisinger T, Wedlich-Söldner R (2011). Cortical actin dynamics driven by formins and myosin V. J Cell Sci 124, 1533–1541.
Yu L, Qi M, Sheff MA, Elion EA (2008). Counteractive control of polarized morphogenesis during mating by mitogen-activated protein kinase Fus3 and G1 cyclin-dependent kinase. Mol Biol Cell 19, 1739–1752.